The Astrophysical Journal, 881:1 (22pp), 2019 August 10 https://doi.org/10.3847/1538-4357/ab2cd4

Global Energetics of Solar Flares. VIII. The Low-energy Cutoff

Markus J. Aschwanden[1], Eduard P. Kontar[2], and Natasha L. S. Jeffrey[2]
[1] Lockheed Martin, Solar and Astrophysics Laboratory, Org. A021S, Bldg. 252, 3251 Hanover St., Palo Alto, CA 94304, USA; aschwanden@lmsal.com
[2] School of Physics and Astronomy, University of Glasgow, Glasgow G12 8QQ, UK; natasha.jeffrey@glasgow.ac.uk
Received 2019 April 24; revised 2019 June 12; accepted 2019 June 21; published 2019 August 6

Abstract

One of the key problems in solar flare physics is the determination of the low-energy cut-off: the value that determines the energy of nonthermal electrons and hence flare energetics. We discuss different approaches to determine the low-energy cut-off in the spectrum of accelerated electrons: (i) the total electron number model, (ii) the time-of-flight model (based on the equivalence of the time-of-flight and the collisional deflection time), (iii) the warm target model of Kontar et al., and (iv) the model of the spectral cross-over between thermal and nonthermal components. We find that the first three models are consistent with a low-energy cutoff with a mean value of $\approx$10 keV, while the cross-over model provides an upper limit for the low-energy cutoff with a mean value of $\approx$21 keV. Combining the first three models we find that the ratio of the nonthermal energy to the dissipated magnetic energy in solar flares has a mean value of $q_E = 0.57 \pm 0.08$, which is consistent with an earlier study based on the simplified approximation of the warm target model alone ($q_E = 0.51 \pm 0.17$). This study corroborates the self-consistency between three different low-energy cutoff models in the calculation of nonthermal flare energies.

Key words: magnetic reconnection – Sun: corona – Sun: flares

Supporting material: machine-readable table

1. Introduction

The ultimate goal of this series of papers is the test of energy closure in solar flares and associated coronal mass ejection (CME) events, which entails the available energies $E_{\rm diss}$ that can be dissipated (magnetic free energy $E_{\rm mag}$, and aerodynamic drag energy $E_{\rm drag}$), and are transformed into primary energy dissipation processes (acceleration of nonthermal particles $E_{\rm nth}$, direct heating $E_{\rm dir}$, and the kinetic energy of a CME, $E_{\rm cme}$), as well as into secondary processes (precipitation-induced thermal energies, and CME-accelerated particles). Statistical results of these energies have been calculated for medium-sized to large flare events (Emslie et al. 2012; Aschwanden et al. 2014, 2015, 2016, 2017; Aschwanden 2016, 2017; Aschwanden & Gopalswamy 2019). For summaries see also Aschwanden (2019). A key result is the statistical energy closure of primary energy dissipation processes, i.e., $(E_{\rm nth} + E_{\rm dir} + E_{\rm cme})/E_{\rm diss} = 0.87 \pm 0.18$ (Aschwanden et al. 2017). The largest amount of the dissipated magnetic energy goes into the acceleration of electrons $E_{\rm nth}/E_{\rm diss} = 0.51 \pm 0.17$. Importantly, the measurement of the nonthermal energy $E_{\rm nth}$ bears the largest uncertainty due to the poorly known low-energy cutoff ε_c, which is the central focus of this study.

The low-energy cutoff problem arises because the instantaneous electron injection spectrum can be approximated with a power-law function $f_e(\varepsilon) \propto \varepsilon^{-\delta}$ above a minimum electron energy ε_c (e.g., in the thick-target model of Brown 1971). The fact that the power-law slope is generally very steep, i.e., $\delta \approx 3$–8 (Dennis 1985), makes the spectrally integrated electron flux extremely sensitive to the accurate value of the low-energy cutoff value ε_c. If we change this cutoff value from $\varepsilon = 10$ keV by a factor of 2 to $\varepsilon = 20$ keV, the electron flux varies by a factor of $\approx 2^{\delta}$, which amounts to 1–2 orders of magnitude. The effects of low-energy cutoffs on solar flare microwave and hard X-ray spectra was investigated in Holman (2003), with the finding that microwave spectra become smoothed in the optically thick portion, while hard X-ray (photon) spectra are flattened below the cutoff energy. Modeling of the thermal spectrum of hard X-ray photons has traditionally been done with an isothermal model (Culhane 1969; Culhane & Acton 1970; Brown 1974a; Holman et al. 2011), while a multi-thermal function involves a more realistic approach and was found to fit the data equally well (e.g., Aschwanden 2007). Moreover, the altitude of the coronal X-ray sources is observed to increase with energy in the thermal range (Jeffrey et al. 2015), so that solar flares are multi-thermal and have strong vertical temperature and density gradients with a broad temperature distribution. The ambiguity between an isothermal and a multi-thermal spectrum contributes to further confusion between the thermal and nonthermal spectral components, so that the spectral cross-over does not reveal the exact cutoff energy, but yields a value that is about a factor of 2 too high. In a previous study on the multi-thermal modeling of 44 flare events, the spectral cross-over was found in the range of $e_{\rm co} = 10$–28 keV, with a mean and standard deviation of $e_{\rm co} = 18.0 \pm 3.4$ keV (Aschwanden 2007).

A new theoretical model based on collisional relaxation and diffusion of electrons in a warm coronal plasma was proposed by Kontar et al. (2015, 2019), which in principle yields the low-energy cutoff $\varepsilon_{\rm wt}$ in a modified thick-target model. This model represents a more realistic approach, because it generalizes the standard cold thick-target model (with a cold plasma target) by including an additional warm plasma "lid" above the cold chromospheric component and, unlike the cold thick target, preserves the number of electrons in the warm plasma. Importantly, the warm target model uses the warm coronal plasma environment (its temperature, number density, and warm plasma extent) to constrain the properties of the accelerated electron distribution. In general, the low-energy cutoff should be determined by fitting the warm target model to the observed X-ray count spectrum (see Kontar et al. 2019). An application of a simplified version of this warm target model to 191 M- and X-class flares yielded a mean low-energy cutoff of $\varepsilon_{\rm wt} = 6.2 \pm 1.6$ keV (Aschwanden et al. 2016), which is significantly lower than the cross-over energy of $\varepsilon_{co} = 21 \pm 6$ keV. It can be shown that the low-energy cutoff in a cold thick-target model is essentially undetermined (e.g., Ireland et al. 2013; Kontar et al. 2019), while it was shown that the warm target model can constrain the low-energy cutoff down to 7% at a 3σ level (Kontar et al. 2019).

Here, we further study the low-energy cutoffs inferred from the warm target model. One issue is that the plasma in a flare is highly inhomogeneous, ranging from the cold background corona values at the beginning of a flare ($T_{cold} \approx 0.5$–2 MK) to the hot chromospheric evaporation component ($T_{hot} \approx 5$–25 MK) at the flare peak time, causing some ambiguity about which temperature to attribute to the warm plasma component that constrains the low-energy cutoff. In the warm target model, the deduction of the coronal plasma environment is crucial for constraining the low-energy cutoff, and hence the nonthermal electron power (Kontar et al. (2019).

Further, we will explore the total number of electrons in a flaring plasma and the spectral cross-over ε_{co} as well as the warm target model ε_{wt} predictions. Moreover, the electron number model ε_{en}, and the electron time-of-flight model ε_{tof} will be applied. The latter two models invoke the equivalence of the collisional deflection time and the electron time-of-flight timescale, as well as the limit of the maximum number of electrons that can be accelerated in a finite flare volume, which at the same time solves the electron number problem.

The content of this paper includes an analytical description and derivation of all four theoretical models of the low-energy cutoff (Section 2), followed by a description of the data analysis and fitting of the theoretical models to the observational data sets of all M- and X-class flares observed with the Atmospheric Imaging Assembly (AIA) and the Helioseismic and Magnetic Imager (HMI) onboard the *Solar Dynamics Observatory* (*SDO*) during 2010–2014, which amounts to 191 solar flare events (Section 3), with a discussion (Section 4) and conclusions (Section 5).

2. Theory

We describe four different models that independently provide theoretical estimates of the low-energy cutoff of a hard X-ray spectrum in solar flares. In the following, we present analytical derivations and assumptions of these models: the electron number model (Section 2.1), the time-of-flight model (Section 2.2), the warm target model (Section 2.3), and the spectral cross-over model (Section 2.4). The first two models are used here for the first time to derive the low-energy cutoff, while the third model was used in Aschwanden et al. (2016), and the fourth model represents a common method to derive upper limits on the low-energy cutoff.

2.1. The Total Electron Number Model

In the thick-target model (Brown 1971, see, e.g., Section 13.2.2 in Aschwanden 2004), the hard X-ray photon spectrum is defined by a power-law function of the observed photon energies ϵ_x,

$$I(\epsilon_x) = I_1 \frac{(\gamma - 1)}{\epsilon_1} \left(\frac{\epsilon_x}{\epsilon_1}\right)^{-\gamma} \quad (\text{photons cm}^{-2}\ \text{s}^{-1}\ \text{keV}^{-1}). \quad (1)$$

The corresponding electron injection spectrum of electrons is

$$f_e(\varepsilon) = 2.68 \times 10^{33}\ (\gamma - 1)\ b(\gamma)\ \frac{I_1}{\epsilon_1^2} \times \left(\frac{\varepsilon}{\epsilon_1}\right)^{-(\gamma+1)} \quad (\text{electrons keV}^{-1}\ \text{s}^{-1}), \quad (2)$$

and has the power-law slope $\delta = \gamma + 1$. The total number of electrons above a cutoff energy ε_c, i.e., $F(\varepsilon \geqslant \varepsilon_c)$, is given by the thick-target model:

$$F(\varepsilon \geqslant \varepsilon_c) = \int_{\varepsilon_c}^{\infty} f_e(\varepsilon)\ d\varepsilon = 2.68 \times 10^{33}\ b(\gamma)\ \frac{(\gamma - 1)}{\gamma} \frac{I_1}{\epsilon_1} \left(\frac{\varepsilon}{\epsilon_1}\right)^{-\gamma} \quad (\text{electrons s}^{-1}), \quad (3)$$

where $b(\gamma)$ is an auxiliary function that contains the beta function $B(p, q)$,

$$b(\gamma) = \gamma^2 (\gamma - 1)^2 B\left(\gamma - \frac{1}{2}, \frac{3}{2}\right), \quad (4)$$

which was calculated by Hudson et al. (1978) for a relevant range of spectral slopes γ of the observed photon spectrum, and was approximated by the function (Aschwanden 2004)

$$b(\gamma) \approx 0.27\ \gamma^3, \quad (5)$$

and ϵ_1 is the reference energy at which the photon flux I_1 is measured.

Now we define the total number of electrons integrated over the total flare duration τ_{flare}:

$$N_e = F(\varepsilon \geqslant \varepsilon_c)\ \tau_{flare} \quad (\text{electrons}). \quad (6)$$

On the other hand, we can assume the total number of accelerated nonthermal electrons during a flare by integrating the preflare electron density n_{e0} over the flare volume $V = L^3 q_{geo}$, where L is an appropriate length scale of a cube that encompasses the entire flare volume:

$$N_e = n_{e0} V = n_{e0}\ L^3\ q_{geo} \quad (\text{electrons}), \quad (7)$$

and q_{geo} is a geometric filling factor of the subvolume that contains the number of electrons that can be accelerated out of the cubic flare volume. We note that this assumption neglects the role of return currents, which will maintain the total number of electrons (e.g., Somov 2000). In other words, the total number of electrons in the flaring region is assumed to be equal to the total number of electrons accelerated above the low-energy cutoff. Even if this approximation is coarse, it gives useful details about the efficiency of electron acceleration in solar magnetic reconnection regions.

In the standard CHSKP flare models for magnetic reconnection (Carmichael 1964; Sturrock 1966; Hirayama 1974; Kopp & Pneuman 1976), the subvolume in which charged particles (electron and ions) are accelerated encompasses about a fraction of $q_{geo} \approx 1/4$ of the cubic flare volume, as can be estimated from the geometry shown in Figure 1 (shaded triangular subvolume). The geometric filling factor consists of a factor of $q_{height} = 1/2$ due to the vertical cusp range, which covers half of the apex height, and an additional factor of $q_{triangle} = 1/2$, which accommodates the ratio of the triangular

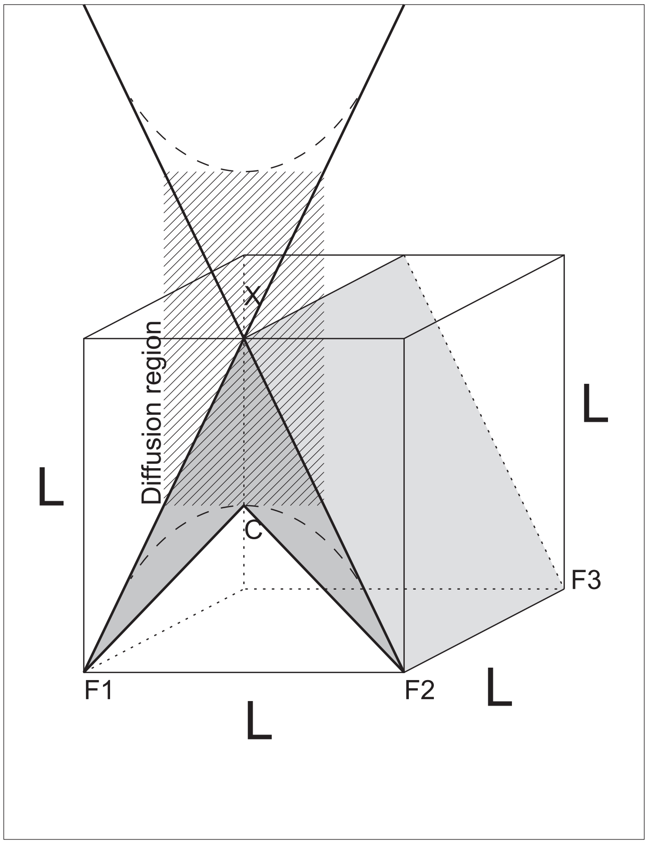

Figure 1. Geometric model of a flare arcade embedded in a cube with length L, width $w = L$, and height $h = L$, with volume $V = L \times w \times h = L^3$. The footpoints of the loop arcade are at the locations $F1$ and $F2$, the X-point X at height $h = L$, and the cusp C at height $L/2$. The magnetic field line through the cusp is approximated with the triangle $F1 - C - F2$ and has the volume $V = L^3 \times q_{\rm geo}$, where the geometric filling factor of the cube is $q_{\rm geo} = 1/4$. The diffusion region of magnetic reconnection in the X-point is indicated with a shaded area and has the same filling factor of $q_{\rm geo} = 1/4$.

arcade cross-section to the encompassing cube volume, resulting in a combined factor of $q_{\rm geo} = q_{\rm height} \times q_{\rm triangle} = (1/2) \times (1/2) = 1/4$. Alternatively, we can estimate the geometric filling factor from the approximate size of the diffusion region of the magnetic reconnection volume, which occupies the half apex height ($h = L/2$) and half of the horizontal footpoint separation ($w_L/2$), and in this way produces the same geometric filling factor of $q_{\rm geo} = (h/L) \times (w/L) = (1/2) \times (1/2) = 1/4$ (hatched area in Figure 1).

Combining the two expressions for the total number of electrons N_e accelerated in a flare (using Equations (1)–(6)) we obtain,

$$N_e = n_e L^3 q_{\rm geo} = 0.72 \times 10^{33}\ \gamma^2(\gamma - 1)\frac{I_1}{\epsilon_1} \times \left(\frac{\varepsilon_{\rm en}}{\epsilon_1}\right)^{-\gamma} \tau_{\rm flare} \quad \text{(electrons)}. \tag{8}$$

Using the normalized unit $L_{10} = L/10^{10}$ cm, we obtain the following simple expression for the low-energy cutoff $\varepsilon_{\rm en}$, where the subscript "en" refers to the electron number model,

$$\varepsilon_{\rm en} = \epsilon_1 \left[\frac{n_{e0}\ L_{10}^3\ q_{\rm geo}\ \epsilon_1}{0.72\ \gamma^2(\gamma - 1)\ I_1\ \tau_{\rm flare}}\right]^{-1/\gamma} \quad \text{(keV)}, \tag{9}$$

which depends on the observables n_{e0}, γ, I_1, ϵ_1, $\tau_{\rm flare}$ and the model parameter $q_{\rm geo} \approx 1/4$. The photon flux I_1 and the spectral power-law slope γ at the energy ϵ_1 can directly be obtained from a hard X-ray spectrum, the flare duration $\tau_{\rm flare}$ can be measured from hard X-ray time profiles, and the electron density n_{e0} has to be estimated before the onset of the flare, which is typically $n_{e0} \approx 10^9$ cm^{-3} (Figure 3(h) below).

Once we have a model for the low-energy cutoff $\varepsilon_{\rm en}$, we can calculate the power in nonthermal electrons above this cutoff energy by integrating the electron energies ε, with $b(\gamma)$ defined in Equations (4) or (5):

$$P_{\rm en}(\varepsilon \geqslant \varepsilon_{\rm en}) = \int_{\varepsilon_{\rm en}}^{\infty} f_e(\varepsilon)\ \varepsilon\ d\varepsilon = 4.3 \times 10^{24}\ b(\gamma) I_1 \left(\frac{\varepsilon_{\rm en}}{\epsilon_1}\right)^{-(\gamma-1)} \quad ({\rm erg\ s^{-1}}) \tag{10}$$

and the total energy $E_{\rm en}$ integrated over the flare duration $\tau_{\rm flare} = (t_2 - t_1)$ is

$$E_{\rm en} = \int_{t_1}^{t_2} P_{\rm en}(\varepsilon \geqslant \varepsilon_{\rm en}, t)\ dt \quad \text{(erg)}, \tag{11}$$

where the photon flux $I_1(t)$, the power-law slope $\gamma(t)$, and the low-energy cutoff energy $\varepsilon_{\rm en}(t)$ are time-dependent.

2.2. The Time-of-flight Model

For stochastic acceleration models with binary Coulomb collisions, where particles gain and lose energy randomly, the collisional mean free path yields an upper limit for the propagation distance of free-streaming electrons. The balance between acceleration and collisions can lead to the formation of a kappa-distribution according to some solar flare models (e.g., Bian et al. 2014). For solar flares, we can thus estimate the critical energy between collisional and collisionless electrons from the collisional deflection time $t_{\rm defl}$ (Benz 1993):

$$t_{\rm defl} \approx 0.95 \times 10^8 \left(\frac{e_{\rm keV}^{3/2}}{n_e}\right)\left(\frac{20}{\ln \Lambda}\right), \tag{12}$$

where $\ln \Lambda \approx 20$ is the Coulomb logarithm. We set the collisional deflection time equal to the (relativistic) time-of-flight propagation time between the coronal acceleration site and the chromospheric thick-target energy loss site:

$$t_{\rm tof} = \frac{L_{\rm tof}}{v} = \frac{L_{\rm tof}}{\beta c}. \tag{13}$$

The relativistic speed $\beta = v/c$,

$$\beta = \sqrt{1 - \frac{1}{\gamma_r^2}}, \tag{14}$$

is related to the kinetic energy $e_{\rm kin}$ of the electron by

$$e_{\rm kin} = m_e c^2(\gamma_r - 1) = 511(\gamma_r - 1) \quad \text{(keV)}, \tag{15}$$

where γ_r represents here the relativistic Lorentz factor (not to be confused with the spectral slope γ used above, i.e., Equation (1)). We are setting these two timescales equal (Aschwanden et al. 2016, Appendix A therein):

$$t_{\rm defl} = t_{\rm tof}, \tag{16}$$

where we use $\ln \Lambda \approx 20$, define the kinetic energy $\epsilon_{\mathrm{keV}} = \epsilon_{\mathrm{kin}}$, and obtain with Equations (12)–(16)

$$(\gamma_r - 1)^{3/2}\left(1 - \frac{1}{\gamma_r^2}\right)^{1/2} = \frac{L_{\mathrm{tof}}\ n_e}{0.95 \times 10^8 \times 511^{3/2} c}. \quad (17)$$

Using the low-relativistic approximation (for $\gamma_r \gtrsim 1$),

$$\begin{aligned}(\gamma_r - 1)^{3/2}\left(1 - \frac{1}{\gamma_r^2}\right)^{1/2} &= (\gamma_r - 1)^{3/2}\frac{(\gamma_r - 1)^{1/2}(\gamma_r + 1)^{1/2}}{\gamma_r}\\ &= \frac{(\gamma_r - 1)^2(\gamma_r + 1)^{1/2}}{\gamma_r} \approx (\gamma_r - 1)^2\sqrt{2}, \quad (18)\end{aligned}$$

we obtain

$$(\gamma_r - 1)^2\sqrt{2} \approx 0.0003 \times \left(\frac{L_{\mathrm{tof}}}{10^{10}\ \mathrm{cm}}\right)\left(\frac{n_e}{10^{10}\ \mathrm{cm}^{-3}}\right). \quad (19)$$

The time-of-flight distance is approximately $L_{\mathrm{tof}} = L\sqrt{2}$, where the flare length scale L is also the vertical extent of the cusp (Figure 1), and the factor $\sqrt{2}$ corrects for the mean pitch angle (45°) of the electrons spiraling along the time-of-flight path. Then, by inserting $(\gamma_r - 1) = e_c/511$ keV from Equation (15), we find the cross-over energy $e_{\mathrm{tof}} \approx e_{\mathrm{kin}}$, explicitly expressed as

$$e_{\mathrm{tof}} \approx 28\left(\frac{L}{10^{10}\ \mathrm{cm}}\right)^{1/2}\left(\frac{n_e}{10^{10}\ \mathrm{cm}^{-3}}\right)^{1/2} \quad (\mathrm{keV}). \quad (20)$$

This expression requires the measurement of a mean length scale $L = A^{1/2}$ of the flare area and an average electron density n_e where flare-accelerated electrons propagate.

From the model of the low-energy cutoff energy $\varepsilon_{\mathrm{tof}}$, we can calculate the power in nonthermal electrons above this cutoff energy by integrating over the electron energies ε:

$$\begin{aligned}P_{\mathrm{tof}}(\varepsilon \geqslant \varepsilon_{\mathrm{tof}}) &= \int_{\varepsilon_{\mathrm{tof}}}^{\infty} f(\varepsilon)\ d\varepsilon\\ &= 4.3 \times 10^{24}\ b(\gamma) I_1\left(\frac{\varepsilon_{\mathrm{tof}}}{\epsilon_1}\right)^{-(\gamma-1)} \quad (\mathrm{erg\ s^{-1}}). \quad (21)\end{aligned}$$

The total energy integrated over the flare duration is then, using the time-dependent functions $\gamma(t)$, $I_1(t)$, and $\varepsilon_{\mathrm{tof}}(t)$,

$$E_{\mathrm{tof}} = \int_{t_1}^{t_2} P_{\mathrm{tof}}(\varepsilon \geqslant \varepsilon_{\mathrm{tof}}, t)\ dt \quad (\mathrm{erg}). \quad (22)$$

Turning the argument around predicts a time-of-flight distance $L_{\mathrm{tof}} \approx \varepsilon_{\mathrm{tof}}^2/n_e$ as a function of the low-energy cutoff $\varepsilon_{\mathrm{tof}}$, which is a similar concept that has been applied to model the size L of the acceleration region as a function of the electron energy e, i.e., $(L - L_0) \propto e^2/n_e$ (Xu et al. 2008; Guo et al. 2012a, 2012b, 2013).

2.3. The Warm-target Model

Previous applications of the thick-target model generally assume cold (chromospheric) temperatures in the electron precipitation site (see, e.g., Holman et al. 2011 for a review). At the same time, the temperature of the flaring solar corona is sufficiently high that finite-temperature effects must be included (Galloway et al. 2005; Goncharov et al. 2010; Jeffrey et al. 2014). Moreover, the slow spatial diffusion of thermalized electrons, previously ignored, led to the theoretical development of the warm target model (Kontar et al. 2015). The model has been tested with numerical simulations that include the effects of collisional energy diffusion, spatial transport, and thermalization of fast electrons (Jeffrey et al. 2014).

The warm target model assumes a two-temperature target plasma (Kontar et al. 2015, 2019): the warm solar corona and the cold chromosphere. The warm corona is collisionally thick to electrons with energy $E < \sqrt{2KnL}$, where $K = 2\pi e^4 \ln \Lambda$ is a constant, n is the density of the coronal plasma, and L is the length of the warm target region. Therefore, the accelerated electrons injected into a flaring loop propagate and collide in the warm plasma. Electrons with energy $E^2 < 2KnL$ lose all of their energy in the coronal plasma and join the Maxwellian distribution of the surrounding plasma, increasing the density of thermal plasma in the loop. The mean electron flux spectrum can be represented by (Kontar et al. 2015)

$$\begin{aligned}\langle nVF\rangle(E) &= \frac{1}{2K} E e^{-E/k_{\mathrm{B}}T} \int_{E_{\min}}^{E} \frac{e^{E'/kT} dE'}{E' G\left(\sqrt{\frac{E'}{k_{\mathrm{B}}T}}\right)} \quad (23)\\ &\quad \times \int_{E'}^{\infty} \dot{N}(E_0) dE_0,\end{aligned}$$

where $G(x) = [\mathrm{erf}(x) - x\ \mathrm{erf}'(x)]/2x^2$. The lower limit in Equation (23) is given by

$$E_{\min} \approx 3k_{\mathrm{B}}T\left(\frac{5\lambda}{L}\right)^4, \quad (24)$$

where $\lambda = (k_{\mathrm{B}}T)^2/2Kn$ is the collisional mean free path, and Equation (24) is determined by considering the warm plasma properties in the corona. The mean electron flux $\langle nVF\rangle(E)$ convolved with the bremsstrahlung cross-section $\sigma(E, \epsilon)$ predicts the X-ray flux spectrum at $R = 1$ au:

$$I(\epsilon) = \frac{1}{4\pi R^2} \int_{E}^{\infty} \langle nVF\rangle(E)\sigma(E, \epsilon) dE \quad (25)$$

where ϵ is the photon energy. Fitting the warm target model X-ray spectrum to the observed X-ray spectrum allows us to determine the parameters of the injected electron flux spectrum, which here is assumed to be a power law:[3]

$$\dot{N}(E) = \dot{N}_0 \frac{\delta - 1}{E_c}\left(\frac{E}{E_c}\right)^{-\delta}, \quad (26)$$

where $\dot{N}_0$ is the electron acceleration rate (electrons s^{-1}), δ is the spectral index, and E_c is the low-energy cut-off in the injected electron spectrum.

The warm target model suggests that electrons are thermalized in the warm plasma of the coronal loop and produce detectable thermal emission with an emission measure of

$$\Delta\mathrm{EM} \approx \frac{\pi}{K}\sqrt{\frac{m_e}{8}}(k_{\mathrm{B}}T)^2 \frac{\dot{N}_0}{E_{\min}^{1/2}}, \quad (27)$$

where ΔEM characterizes the additional contribution to the soft X-ray emission measure from the thermalized accelerated

[3] A warm target kappa model is also available in OSPEX (see Kontar et al. 2019).

electrons. These hot Maxwellian electrons can diffusively escape from the warm plasma of the loop and collisionally stop in the dense cold chromosphere. High-energy electrons with $E^2 > 2KnL$ behave in the same way as in the standard cold thick-target model. It is important to note that the warm target model is responsible for the nonthermal component, and for a fraction of the thermal component of the X-ray emission. The pile-up of low-energy electrons thermalized in the flaring corona allows us to solve the low-energy cut-off problem (Kontar et al. 2019) by comparing the thermalized electrons, that is, by determining the contribution from Equation (27) and the observed X-ray spectrum. In other words, if the low-energy cutoff is determined too low (i.e., if the contribution from ΔEM is too large), then the warm target model produces too many thermalized electrons and hence can be ruled out.

According to the warm target model of Kontar et al. (2015), the effective low-energy cutoff $E_c \simeq \varepsilon_{\rm wt}$ can be coarsely approximated as

$$\varepsilon_{\rm wt} \approx (\xi + 2) k_{\rm B} T_e = \delta\, k_{\rm B} T_e, \tag{28}$$

where $\xi = \gamma - 1$ is the power-law slope of the source-integrated mean electron flux spectrum (see Equations (8)–(10) in Kontar et al. 2015), and T_e is the temperature of the warm target plasma. For medium-sized to large X-class flares, this temperature range spans $T_e \approx$ 10–30 MK, giving (in energy units) $e_{\rm th} = k_{\rm B} T_e =$ 0.9–2.6 keV, and for a typical value of the photon spectral slope $\delta = \gamma + 1 \approx 4$, low-energy cutoffs of $e_{\rm th} = \delta k_{\rm B} T_e \approx$ 3.5–8.5 keV are predicted. In this simplified version, Kontar et al. (2015) stress that the value of T_e used must be that corresponding to the Maxwellian thermal plasma in the loop.

Further, we stress that Equation (28) is determined by considering the energy at which the systematic energy loss rate vanishes in the Fokker–Planck equation governing the evolution of $\langle nVF \rangle$ in a warm plasma, and that an accurate determination of the properties of the accelerated electron distribution can only be determined using the combination of X-ray spectroscopy and imaging outlined in detail in Kontar et al. (2019). We note that, while Equation (28) is an approximation only, it does allow for a relatively robust statistical analysis (Aschwanden et al. 2017), while the detailed fitting outlined in Kontar et al. (2019) is challenging for a large number of flare events. However, the detailed fitting procedure of Kontar et al. (2019), which constrains the plasma parameters T_e, n, and L, is the recommended method to determine the nonthermal electron properties in an individual flare. Here, the use of Equation (28) is likely to provide a lower limit of $e_{\rm th}$, but is still useful for the purpose of a large statistical study.

From the low-energy cutoff approximation $\varepsilon_{\rm wt}$, we can calculate the power in the electron flux $P_{\rm wt}$:

$$\begin{aligned} P_{\rm wt}(\varepsilon \geqslant \varepsilon_{\rm wt}) &= \int_{\varepsilon_{\rm wt}}^{\infty} f(\varepsilon)\, d\varepsilon \\ &= 4.3 \times 10^{24}\, b(\gamma) I_1 \times \left(\frac{\varepsilon_{\rm wt}}{\epsilon_1}\right)^{-(\gamma-1)} \quad (\mathrm{erg\ s^{-1}}) \end{aligned} \tag{29}$$

and the total energy integrated over the flare duration is

$$E_{\rm wt} = \int_{t_1}^{t_2} P_{\rm wt}(\varepsilon \geqslant \varepsilon_{\rm wt}, t)\, dt. \tag{30}$$

2.4. The Spectral Cross-over Model

The bremsstrahlung spectrum $I(\varepsilon)$ of a thermal plasma with electron temperature T_e, as a function of the photon energy $\varepsilon = h\nu$ (with h the Planck constant and ν the frequency), setting the coronal electron density equal to the ion density ($n = n_i = n_e$), and neglecting factors of the order of unity (such as the Gaunt factor $g(\nu, T)$ in the approximation of the Bethe–Heitler bremsstrahlung cross-section), and the ion charge number, $Z \approx 1$, is (Brown 1974b; Dulk & Dennis 1982),

$$I(\varepsilon) = I_0 \int \frac{\exp(-\varepsilon/k_{\rm B}T)}{T^{1/2}} \frac{dEM(T)}{dT}\, dT, \tag{31}$$

where $I_0 \approx 8.1 \times 10^{-39}$ keV cm^{-2} s^{1} keV^{-1} and $dEM(T)/dT$ specifies the differential emission measure (DEM) $n^2 dV$ in the volume dV corresponding to a temperature range of dT,

$$\left(\frac{dEM(T)}{dT}\right) dT = n^2(T)\, dV. \tag{32}$$

Regardless of whether we define this DEM distribution by an isothermal or a multi-thermal plasma (Aschwanden 2007), the thermal spectrum $I(\varepsilon)$ falls off similarly to an exponential function at an energy of $\varepsilon \lesssim 20$ keV (or up to $\lesssim$40) keV in extremal cases), while the nonthermal spectrum in the higher-energy range of $\varepsilon \approx$ 20–100 keV can be approximated by a single (or broken) power-law function (Equation (3)).

Because of the two different functional shapes, a cross-over energy $\varepsilon_{\rm co}$ can be defined by the change in the spectral slope between the thermal and the nonthermal spectral component. The electron energy spectrum, however, can have a substantially lower or higher cutoff energy (e.g., Holman 2003). We represent the combined spectrum with the sum of the (exponential-like) thermal and the (power-law-like) nonthermal component, i,e.,

$$\begin{aligned} I(\varepsilon) &= I_{\rm th}(\varepsilon) + I_{\rm nth}(\varepsilon) = I_0 \int \frac{\exp(-\varepsilon/k_{\rm B}T)}{T^{1/2}} \frac{dEM(T)}{dT} \\ &\quad + I_1 \frac{(\gamma-1)}{\epsilon_1} \left(\frac{\epsilon_x}{\epsilon_1}\right)^{-\gamma}, \end{aligned} \tag{33}$$

where the cross-over energy $\varepsilon_{\rm co}$ can be determined in the (best-fit) model spectrum $I(\varepsilon)$ from the energy where the logarithmic slope is steepest, i.e., from the maximum of $\partial \log I(\varepsilon)/\partial \log \varepsilon$. The change of the spectral slope between the thermal and the nonthermal component is depicted in Figure 2, where cross-over energy of $\varepsilon_{\rm co} = 4.7$ keV for a small flare is calculated, and $\varepsilon_{\rm co} = 19.5$ keV for a large flare.

From the low-energy cutoff $\varepsilon_{\rm co}$ we can calculate the power in the electron flux $P_{\rm co}$:

$$\begin{aligned} P_{\rm co}(\varepsilon \geqslant \varepsilon_{\rm co}) &= \int_{\varepsilon_{\rm co}}^{\infty} f(\varepsilon)\, d\varepsilon \\ &= 4.3 \times 10^{24}\, b(\gamma) I_1 \left(\frac{\varepsilon_{\rm co}}{\epsilon_1}\right)^{-(\gamma-1)} \quad (\mathrm{erg\ s^{-1}}), \end{aligned} \tag{34}$$

and the total energy integrated over the flare duration is

$$E_{\rm co} = \int_{t_1}^{t_2} P_{\rm co}(\varepsilon \geqslant \varepsilon_{\rm co}, t)\, dt. \tag{35}$$

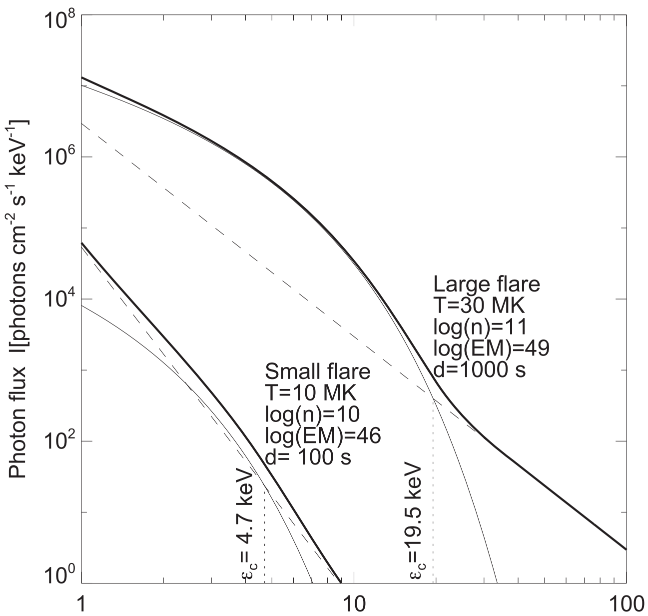

Figure 2. Theoretical hard X-ray spectrum consisting of a thermal and a nonthermal (power-law) component with equal energy content above the cutoff energy ε_c. The parameters are chosen for a large flare with $T_e = 30$ MK, $n_e = 10^{11}$ cm^{-3}, $\mathrm{EM}_V = 10^{49}$ cm^{-3}, $\gamma = 3$, and duration $\tau_{\rm flare} = 1000$ s; and for a small flare with $T_e = 10$ MK, $n_e = 10^{10}$ cm^{-3}, $\mathrm{EM}_V = 10^{46}$ cm^{-3}, $\gamma = 5$, and duration $\tau_{\rm flare} = 100$ s. The x-axis is the photon energy in units of keV.

We should be aware that the so-determined cross-over energy $\varepsilon_{\rm co}$ is an upper limit only, and consequently the total energy $E_{\rm co}$ is a lower limit, unlike the other three low-energy cutoff models described in Sections 2.1–2.3.

3. Observations and Data Analysis

The previously analyzed data set is based on all M- and X-class flares observed with the AIA (Lemen et al. 2012) and the HMI (Scherrer et al. 2012) onboard the *SDO* spacecraft (Pesnell et al. 2011) during 2010–2014, which amounts to 399 solar flare events. Here we use only those events that have been simultaneously observed with the *Ramaty High Energy Solar Spectroscopic Imager* (*RHESSI*; Lin et al. 2002), which amount to 191 events, due to the duty cycle of ≈50% of *RHESSI* when the orbit is on the sunward side.

3.1. Spectral Modeling of RHESSI Data

We use the same *RHESSI* data of 191 flare events as previously analyzed in Aschwanden et al. (2016), using the OSPEX (Object Spectral Executive) software (http://hesperia.gsfc.nasa.gov/). We re-analyzed the *RHESSI* data by optimizing the flare time intervals and the energy intervals (typically in the fitting range of $\varepsilon \approx 10$–30 keV) and obtained essentially the same results as described in Aschwanden et al. (2016). The observed hard X-ray photon spectrum has been fitted with an isothermal component (defined by the emission measure EM_{49} in units of 10^{49} (cm^{-3}) and the temperature T_e in units of MK), plus a nonthermal component with a broken power-law function (defined by the nonthermal flux I_1 in units of photons cm^{-2} s^{-1} keV^{-1} at a reference energy of $\epsilon_1 = 50$ keV, and by the power-law index δ of the fitted (lower) electron spectrum, which corresponds to a power-law index of $\gamma = \delta - 1$ in the thick-target model. Examples of such two-component (thermal plus nonthermal) hard X-ray photon spectra are illustrated in Figure 2. The hard X-ray spectra are fitted in time intervals of $\Delta t = 20$ s and yield the time-dependent best-fit parameters $\mathrm{EM}_{49}(t)$, $T_e(t)$, $I_{\rm nth}(t)$, and $\delta(t)$. The maximum values of the emission measure EM_{49}, the temperature $T_e^{\rm rhessi}$, and the photon flux $I_1(t)$, during the flare duration $\tau_{\rm flare}$, as well as the minimum value of the spectral slope $\gamma = \delta - 1$, are listed in Table 2 for 160 (out of the 191) available events (omitting the less reliable cases with data gaps or inaccurate fits that result in outliers with extreme nonthermal energies of $E_{\rm nth} > 10^{33}$ erg). A summary of the parameter ranges is given in Table 1. More details of the spectral modeling of *RHESSI* data are given in Section 3.1 in Aschwanden et al. (2016).

3.2. DEM Modeling

Besides the hard X-ray spectral modeling, we need also to measure the parameters of the spatial length scale L, the electron temperature T_e, and the electron density n_e during the preflare phase as well as during the flare. The preflare electron density n_{e0} and the mean flare electron density n_e are listed in the three last columns of Table 2, i.e., labeled as $b_{10} = n_e^{\rm bg}/10^{10}$ for the background and $n_{10} = n_e^{\rm flare}/10^{10}$ during the flare.

The spatial length scale L has been deduced from measuring the flare area $A(t) = L(t)^2$, subject to corrections due to projection effects and electron density scale heights λ (Aschwanden et al. 2014, 2015), where the flare volume V is approximated by the Euclidean relationship

$$V = L^3. \qquad (36)$$

From DEM modeling of the EUV data (observed with AIA) earlier (Aschwanden et al. 2015), we obtained the emission measure $\mathrm{EM}_{\rm EUV}$ of the ("cold" and "warm") flare plasma and emission-measure-weighted temperature ($T_{\rm EUV}$), and the corresponding electron density ($n_{\rm EUV}$):

$$n_{\rm EUV} = \sqrt{\frac{\mathrm{EM}_{\rm EUV}}{V}}, \qquad (37)$$

measured at the peak time of the nonthermal hard X-ray flux.

In addition, the thermal emission measure (EM_R) and temperature T_R of the hot" flare plasma have been measured from the two-component (thermal and nonthermal) spectral fit to the *RHESSI* data, but we should be aware that the *RHESSI*-inferred values are always biased toward the hottest temperature component. Nevertheless, the corresponding electron density n_R is then defined by the relationship during the flare at times t:

$$n_R(t) = \sqrt{\frac{\mathrm{EM}_R(t)}{V}}. \qquad (38)$$

Measuring the density at the starting time of the flare ($t = t_1$) yields then also an estimate of the preflare (or background) density ($n_{\rm bg}$)

$$n_{\rm bg} = n_R(t = t_1) = \sqrt{\frac{\mathrm{EM}_R(t_1)}{V}}. \qquad (39)$$

This preflare density $n_{\rm bg}$ is used in the electron number model (Section 2.1), where the maximum possible number of accelerated electrons in the full flare volume (essentially defined by the envelope volume of the entire flare arcade) during the preflare phase corresponds to the partial volume $V = L^3 q_{\rm geo}$ (Equation (6)), with a geometric filling factor

Table 1
Ranges, Medians, Means and Standard Deviations, and Variance Ratios of the Observed Variables in the Determination of the Low-energy Cutoff ε_c Listed According to Figure 2, for a Total of 191 M- and X-class Flares

Parameter	Minimum $x_{\rm min}$	Median $x_{\rm med}$	Maximum $x_{\rm max}$	Mean Std $x_{\rm mean} \pm \sigma$	Variance Ratio $\sigma/x_{\rm mean}$
Temperature T_e (MK)	3.4	12.5	33.7	13.5 ± 5.4	1.40
Spectral slope γ	2.8	7.2	10.4	7.0 ± 1.4	1.20
Length scale L (Mm)	1.7	9.8	34.8	10.9 ± 6.0	1.55
Flare duration t_{flare} (s)	$10^{2.20}$	$10^{3.22}$	$10^{3.98}$	$10^{3.2 \pm 0.27}$	1.84
Emission measure EM (cm^{-3})	$10^{44.3}$	$10^{47.0}$	$10^{51.4}$	$10^{47.1 \pm 1.04}$	11.0
Photon flux I_1 (photons cm^{-2} s^{-1} keV^{-1})	$10^{-5.12}$	$10^{-3.34}$	$10^{-0.65}$	$10^{-3.27 \pm 0.81}$	6.40
Flare electron density n_e	$10^{8.30}$	$10^{9.97}$	$10^{12.13}$	$10^{10.1 \pm 0.80}$	3.69
Preflare electron density n_{e0}	$10^{8.00}$	$10^{9.34}$	$10^{13.41}$	$10^{9.60 \pm 0.80}$	6.34

$q_{\rm geo} = 1/4$ derived from the geometry of the diffusion region in a 3D magnetic reconnection process with propagation of the hard X-ray footpoints along a flare ribbon with an approximative length L.

In the time-of-flight model (Section 2.2) we need an electron density n_e that is representative of the hot evaporating plasma, where electrons are stopped by collisional deflection. For this regime we use the emission measure $\mathrm{EM}_R(t)$ and temperature $T_R(t)$ obtained from the spectral fitting of the thermal component observed with *RHESSI*.

In the warm target model (Section 2.3) we need an electron temperature that is characteristic for the "warm" target region (from the acceleration region to the top of the chromosphere), where the thermalization of fast electrons takes place. We estimate this intermediate temperature from the geometric mean of the "warm" plasma observed in EUV (used in the DEM analysis) and the "hot" thermal plasma seen by *RHESSI*:

$$T_e(t_p) = [T_{\rm EUV} \times T_R(t_p)]^{1/2}. \tag{40}$$

The temperature during the peak time t_p of the nonthermal hard X-ray flux is listed in Table 2, and a histogram is shown in Figure 3(a), which reveals a typical range of $T_e \approx$ 5–30 MK.

3.3. Statistical Results

The statistical distributions of the observables are shown in the form of histograms on a linear or logarithmic scale in Figure 3 and are listed in Tables 1 and 3. The median values are: $T_e \approx 12.5$ MK for the maximum electron temperature (defined by the geometric mean between the EUV-inferred ($T_{\rm EUV}$) and *RHESSI*-inferred (T_R) values); $\gamma \approx 7$ for the photon spectral index; $L \approx 10$ Mm for the spatial flare length scale; $\tau_{\rm flare} \approx 0.5$ hr for the flare duration (defined by the time difference between *GOES* start and peak times); EM $\approx 1 \times 10^{47}$ cm^{-3} for the emission measure observed by *RHESSI*; $F \approx 5 \times 10^{-4}$ (photons cm^{-2} s^{-1} keV^{-1}) for the photon flux at $\epsilon_1 = 50$ keV; $n_{\rm eo} \approx 1 \times 10^{10}$ cm^{-3} for the preflare electron density; and $n_e \approx 2 \times 10^{10}$ cm^{-3} for the maximum flare electron density.

The statistical results of this analysis consist of the low-energy cutoffs ε_c and the total nonthermal energies $E_{\rm nth}$ of 191 M- and X-class flares for all four theoretical models, which are tabulated in Figure 3, while the size distribution of the low-energy cutoffs are displayed in Figure 4, and the size distributions of nonthermal energies are shown in Figure 5.

The size distributions of the low-energy cutoffs shown in Figure 4 reveal almost identical median values for the first three models: $\varepsilon_{\rm en} = 10.8$ keV for the electron number model (Figure 4(a)), $\varepsilon_{\rm tof} = 9.8$ keV for the time-of-flight model (Figure 4(b)), and $\varepsilon_{\rm wt} = 9.1$ keV for the warm target model (Figure 4(c)), while the cross-over model reveals a value that is a factor of 2 higher, i.e., $\varepsilon = 21$ keV, which clearly corroborates the theoretical expectation that the spectral cross-over represents an upper limit on the low-energy cutoff only. Now we have a quantitative result that the low-energy cutoff is overestimated by a factor of 2, statistically. This has the consequence that the nonthermal energy is underestimated by about a factor of about $2^4 = 16$ (for an electron power index of $\delta \approx 4$).

The size distributions of the nonthermal flare energies of the analyzed 191 flare events are displayed in Figure 5, for each of the four low-energy cutoff models separately. The most conspicuous difference between the different theoretical models is that the cross-over model is not able to produce nonthermal energies above $E_{\rm nth} \gtrsim 2 \times 10^{30}$ erg, while the other three models all can produce energies up to $E_{\rm nth} \lesssim 10^{33}$ erg. This is consistent with the expected bias that upper limits of the low-energy cutoff substantially underestimate the spectral integrated energy for the cross-over model, because the nonthermal energy scales with a very high nonlinear power (typically with a power index of $\delta \approx 4$). There are additional differences in the size distributions, especially regarding the power-law index of the slope. The electron number model produces a negative power-law slope of $\alpha \approx 1.4$, which is closest to most energy distributions of solar flares among the first three models shown in Figure 5 (e.g., $\alpha_E = 1.53$; Crosby et al. 1993). The warm target model produces a surprisingly flat power-law slope, with $\alpha \approx 1.1$, probably because of a systematic overestimation of the nonthermal energy of large flares. It is possible that the functional form of the low-energy cutoff spectrum, for which traditionally a step function at the lower boundary ε_c is assumed (e.g., Holman 2003), may be unrealistic. A smoother function for the boundary would steepen the power-law slopes of the size distributions for the warm target model and the time-of-flight model, and this would bring them closer to the canonical value of $\alpha_E \approx 1.5$ observed in nonthermal energies (e.g., Crosby et al. 1993; see Table 3 in Aschwanden 2015).

3.4. Nonthermal Energy versus Dissipated Magnetic Energy

The main focus of this series of studies is the global energetics and energy partition in solar flares and CMEs. One

Table 2
Observables of Flare Hard X-Ray Emission in 143 M- and X-class Flare Events

ID	Date	Time	*GOES* Class	Heliogr. Position	Dur. Flare $\tau_{\rm flare}$ (s)	Emission Measure EM_{49} (cm^{-3})	Temp. Max. T_e (MK)	Photon Flux I_1 ($\mathrm{cm}^2\ \mathrm{s\ keV}^{-1}$)	Spectral Slope γ	Length Scale L (Mm)	Density Maximum n_{10} (cm^{-3})	Density Preflare b_{10} (cm^{-3})
1	2010 Jun 12	0030	M2.0	N23W47	904	0.00428	10.73	0.0000736	4.24	13.23	0.43	0.18
2	2010 Jun 13	0530	M1.0	S24W82	1852	0.00002	12.67	0.0000181	5.04	12.25	0.03	0.01
3	2010 Aug 7	1755	M1.0	N13E34	3700	0.00005	12.03	0.0007735	4.09	25.10	0.02	1.64
4	2010 Oct 16	1907	M2.9	S18W26	1572	0.03886	18.18	0.0004585	8.06	15.13	1.06	0.08
10	2011 Feb 13	1728	M6.6	S21E04	2324	0.01753	19.21	0.0088956	7.10	15.94	0.66	0.03
12	2011 Feb 15	0144	X2.2	S21W12	2628	0.24398	21.25	0.0443819	7.06	28.41	1.03	0.13
13	2011 Feb 16	0132	M1.0	S22W27	1368	0.00240	18.71	0.0007753	6.83	12.16	0.37	0.14
15	2011 Feb 16	1419	M1.6	S23W33	1692	0.01667	12.12	0.0003076	7.54	10.74	1.16	0.33
16	2011 Feb 18	0955	M6.6	S21W55	1780	0.09996	9.70	0.0083943	7.21	10.61	2.89	0.15
18	2011 Feb 18	1259	M1.4	S20W70	1944	0.01476	13.66	0.0006862	7.13	6.44	2.35	0.60
19	2011 Feb 18	1400	M1.0	N17E04	1264	0.01366	6.92	0.0002906	4.33	9.43	1.28	0.21
20	2011 Feb 18	2056	M1.3	N15E00	884	0.01607	7.51	0.0001562	7.99	8.43	1.64	0.13
21	2011 Feb 24	0723	M3.5	N14E87	3332	0.01042	10.86	0.0000111	9.23	20.02	0.36	0.06
22	2011 Feb 28	1238	M1.1	N22E35	732	0.00133	8.45	0.0013909	6.51	10.20	0.35	0.26
23	2011 Mar 7	0500	M1.2	N23W47	1340	0.00166	8.11	0.0004404	7.35	5.98	0.88	0.88
28	2011 Mar 7	1943	M3.7	N30W48	3196	0.00172	10.61	0.0029535	5.13	26.55	0.10	0.03
29	2011 Mar 7	2145	M1.5	S17W82	1232	0.00071	10.31	0.0023961	5.78	5.73	0.61	0.04
30	2011 Mar 8	0224	M1.3	S18W80	1460	0.01306	4.13	0.0008550	6.69	9.31	1.27	0.19
31	2011 Mar 8	0337	M1.5	S21E72	2768	8.46763	5.67	0.0000492	8.15	23.95	7.85	0.09
33	2011 Mar 8	1808	M4.4	S17W88	848	0.00494	22.02	0.0023009	7.52	16.21	0.34	0.00
34	2011 Mar 8	1946	M1.5	S19W87	6044	0.00313	8.75	0.0000175	9.16	16.40	0.27	20.96
37	2011 Mar 9	2313	X1.5	N10W11	1660	0.04176	13.88	0.0776128	6.05	34.75	0.32	0.01
38	2011 Mar 10	2234	M1.1	S25W86	1588	0.01840	7.67	0.0001338	7.66	5.74	3.12	0.56
40	2011 Mar 14	1930	M4.2	N16W49	2308	0.21034	10.88	0.0041197	6.88	11.74	3.61	0.26
41	2011 Mar 15	0018	M1.0	N11W83	1500	0.02256	8.97	0.0011179	5.04	4.58	4.85	3.10
46	2011 Apr 22	0435	M1.8	S19E40	3124	0.00986	12.04	0.0006550	6.89	15.75	0.50	0.13
48	2011 May 28	2109	M1.1	S21E70	2848	0.01151	11.79	0.0002199	7.07	11.97	0.82	0.00
50	2011 Jun 7	0616	M2.5	S22W53	3608	5.21387	7.35	0.0019885	3.96	19.91	8.13	0.09
51	2011 Jun 14	2136	M1.3	N14E77	2356	0.00375	10.90	0.0002383	7.37	12.63	0.43	1.63
52	2011 Jul 27	1548	M1.1	N20E41	2004	0.00454	11.38	0.0000151	8.96	16.68	0.31	0.28
53	2011 Jul 30	0204	M9.3	N16E35	1460	0.53662	17.06	0.0063472	7.86	16.20	3.55	0.11
55	2011 Aug 3	0308	M1.1	N15W23	2760	0.00503	12.88	0.0002445	7.64	8.66	0.88	0.00
61	2011 Aug 9	0748	X6.9	N20W69	2256	0.17734	25.80	0.2225979	7.38	28.85	0.86	0.39
63	2011 Sep 5	0408	M1.6	N18W87	1516	0.00075	14.56	0.0000897	7.97	6.80	0.49	0.30
64	2011 Sep 5	0727	M1.2	N18W87	2464	0.00236	14.00	0.0000076	8.38	5.55	1.18	1.41
65	2011 Sep 6	0135	M5.3	N15W03	692	0.02325	10.01	0.0010473	8.42	19.15	0.58	0.05
68	2011 Sep 8	1532	M6.7	N17W39	1764	0.11622	20.71	0.0022988	8.36	16.92	1.55	1.16
69	2011 Sep 9	0601	M2.7	N14W48	1644	0.02375	9.37	0.0018086	7.23	17.19	0.68	0.09
70	2011 Sep 9	1239	M1.2	N15W50	408	0.00262	11.99	0.0000095	9.44	8.41	0.66	1.41
71	2011 Sep 10	0718	M1.1	N14W64	2488	0.00082	21.01	0.0001596	7.87	9.60	0.30	0.00
77	2011 Sep 23	2348	M1.9	N12E56	1020	0.00323	10.26	0.0003025	7.46	15.63	0.29	0.06
81	2011 Sep 24	1719	M3.1	N13E54	1324	0.01758	9.39	0.0007469	7.58	7.20	2.17	0.12
83	2011 Sep 24	1909	M3.0	N15E50	1068	0.01551	8.75	0.0003280	7.79	23.56	0.34	0.69
84	2011 Sep 24	2029	M5.8	N13E52	1180	0.08850	9.40	0.0119517	5.98	11.05	2.56	0.38
86	2011 Sep 24	2345	M1.0	S28W66	1596	0.00126	13.44	0.0000355	7.78	6.99	0.61	0.28
91	2011 Sep 25	1526	M3.7	N15E39	676	0.01059	8.55	0.0001207	8.83	13.64	0.65	3.75
98	2011 Oct 2	0037	M3.9	N10W13	3696	0.01836	12.14	0.0005113	8.25	19.25	0.51	0.01
100	2011 Oct 20	0310	M1.6	N18W88	1044	0.00580	19.18	0.0003065	7.98	7.15	1.26	0.03
101	2011 Oct 21	1253	M1.3	N05W79	760	0.02016	7.03	0.0000893	7.04	6.49	2.72	0.02
103	2011 Oct 31	1455	M1.1	N20E88	3980	0.00846	19.72	0.0007398	7.08	4.23	3.34	1.09
111	2011 Nov 5	1110	M1.1	N22E43	2392	0.00081	17.51	0.0001009	7.74	8.28	0.38	0.21
116	2011 Nov 15	0903	M1.2	N21W72	2448	0.00132	8.89	0.0000964	8.20	7.31	0.58	0.00
120	2011 Dec 26	0213	M1.5	S18W34	2812	0.01884	7.57	0.0000523	7.93	13.91	0.84	0.38
122	2011 Dec 29	1340	M1.9	S25E70	2368	0.00718	15.36	0.0000902	8.09	14.63	0.48	0.08
123	2011 Dec 29	2143	M2.0	S25E67	632	0.00215	15.03	0.0002077	7.91	11.86	0.36	0.07
125	2011 Dec 31	1309	M2.4	S25E46	1892	0.00399	20.88	0.0010953	7.05	8.39	0.82	2.09
126	2011 Dec 31	1616	M1.5	S22E42	1272	0.00323	13.83	0.0001025	8.23	11.86	0.44	0.50
157	2012 Apr 27	0815	M1.0	N13W26	732	0.00757	11.47	0.0000452	8.65	15.58	0.45	0.00
158	2012 May 5	1319	M1.4	N11E78	200	0.00455	13.05	0.0009992	5.76	9.13	0.77	0.10
159	2012 May 5	2256	M1.3	N11E73	624	0.02909	17.36	0.0011669	6.71	7.86	2.45	0.87
160	2012 May 6	0112	M1.1	N11E73	1684	0.02905	3.53	0.0017250	5.94	6.80	3.04	3.19

Table 2
(Continued)

ID	Date	Time	*GOES* Class	Heliogr. Position	Dur. Flare $\tau_{\rm flare}$ (s)	Emission Measure EM_{49} (cm^{-3})	Temp. Max. T_e (MK)	Photon Flux I_1 (cm^2 s keV^{-1})	Spectral Slope γ	Length Scale L (Mm)	Density Maximum n_{10} (cm^{-3})	Density Preflare b_{10} (cm^{-3})
167	2012 May 10	0411	M5.7	N12E19	1128	0.01389	12.02	0.0196674	3.42	15.73	0.60	12.43
168	2012 May 10	2020	M1.7	N12E10	1612	0.00354	12.89	0.0019588	6.47	11.93	0.46	0.10
169	2012 May 17	0125	M5.1	N07W88	2708	0.07451	11.12	0.0002291	7.96	31.30	0.49	0.54
170	2012 Jun 3	1748	M3.3	N15E33	852	0.08183	3.70	0.0009645	4.13	17.31	1.26	2.42
173	2012 Jun 9	1645	M1.8	S16E76	1724	0.01346	7.86	0.0002785	8.03	7.50	1.79	0.09
176	2012 Jun 14	1252	M1.9	S19E06	9628	0.02703	11.25	0.0011941	4.24	6.13	3.43	2.87
178	2012 Jun 29	0913	M2.2	N15E37	696	0.03472	10.61	0.0001820	7.65	8.67	2.31	0.21
182	2012 Jul 2	0026	M1.1	N15E01	1356	0.00326	12.41	0.0001100	7.72	10.32	0.54	0.85
187	2012 Jul 4	0947	M5.3	S17W18	2416	0.02938	13.49	0.0078143	7.05	10.47	1.60	0.93
189	2012 Jul 4	1435	M1.3	S18W20	428	0.02698	12.00	0.0022213	3.38	7.08	2.76	1.17
190	2012 Jul 4	1633	M1.8	N14W33	828	0.01311	12.15	0.0041792	2.76	19.31	0.43	3.14
195	2012 Jul 5	0325	M4.7	S18W29	1768	0.03276	9.85	0.0114881	6.97	8.49	2.31	0.75
196	2012 Jul 5	0649	M1.1	S17W29	1208	0.00287	11.82	0.0002549	7.40	8.11	0.73	0.30
199	2012 Jul 5	1139	M6.1	S18W32	1056	0.02275	12.28	0.0028190	6.09	15.74	0.76	0.24
200	2012 Jul 5	1305	M1.2	S18W36	1400	0.00002	17.10	0.0003799	4.58	13.83	0.03	5.73
203	2012 Jul 6	0137	M2.9	S18W43	2748	0.02383	12.65	0.0007113	8.18	8.49	1.97	0.22
205	2012 Jul 6	0817	M1.5	S12W48	1392	0.01546	14.20	0.0027188	5.80	6.86	2.19	3.25
208	2012 Jul 6	1848	M1.3	S15E88	1348	0.00546	14.39	0.0008365	7.04	10.17	0.72	0.43
210	2012 Jul 7	0310	M1.2	S17W55	1664	0.00597	18.70	0.0009195	6.95	8.67	0.96	0.10
211	2012 Jul 7	0818	M1.0	S16E76	684	0.00182	15.12	0.0000672	6.89	5.01	1.20	1.42
212	2012 Jul 7	1057	M2.6	S17W59	520	0.01474	21.63	0.0022574	7.19	9.37	1.34	50.14
214	2012 Jul 8	0944	M1.1	S16W70	768	0.00198	16.29	0.0001030	8.15	8.49	0.57	0.00
215	2012 Jul 8	1206	M1.4	S16W72	160	0.01743	14.30	0.0029128	6.26	6.38	2.59	1.67
219	2012 Jul 10	0605	M2.0	S16E30	1848	0.00205	18.43	0.0006706	7.18	9.37	0.50	0.50
223	2012 Jul 19	0417	M7.7	S20W88	8532	0.11691	11.72	0.0023355	6.38	17.69	1.45	0.01
228	2012 Aug 6	0433	M1.6	S14E88	728	0.04923	6.39	0.0022234	5.19	4.33	7.79	1.42
230	2012 Aug 17	1312	M2.4	N18E88	1512	0.05884	17.53	0.0006027	7.62	4.99	6.88	0.92
235	2012 Aug 18	2246	M1.0	N18E88	1036	0.00188	12.60	0.0000531	8.48	8.99	0.51	0.33
238	2012 Sep 6	0406	M1.6	N04W61	2184	0.01730	22.22	0.0000244	9.41	9.46	1.43	5.75
241	2012 Sep 30	0427	M1.3	N12W81	2228	0.00236	9.32	0.0009274	7.16	4.94	1.40	22.21
245	2012 Oct 20	1805	M9.0	S12E88	2116	0.08375	10.51	0.0036557	8.14	9.81	2.98	0.25
246	2012 Oct 21	1946	M1.3	S13E78	2124	0.01076	19.52	0.0004559	7.47	9.81	1.07	0.14
248	2012 Oct 23	0313	X1.8	S13E58	1380	0.01599	26.74	0.0562808	6.90	10.40	1.19	0.00
251	2012 Nov 12	2313	M2.0	S25E48	2124	0.03314	8.28	0.0002480	8.21	8.45	2.34	1.33
253	2012 Nov 13	0542	M2.5	S26E44	1396	0.02954	21.22	0.0003934	8.13	10.06	1.70	1.22
255	2012 Nov 14	0359	M1.1	S23E27	1352	0.03191	6.93	0.0014156	3.44	5.17	4.81	3.19
257	2012 Nov 20	1921	M1.6	N10E19	372	0.04471	7.90	0.0007343	4.91	8.61	2.65	0.18
258	2012 Nov 21	0645	M1.4	N10E12	932	0.02454	9.04	0.0008045	6.36	11.93	1.20	0.08
261	2012 Nov 27	2105	M1.0	S13W42	1668	0.00753	14.83	0.0001938	7.99	7.09	1.45	0.22
262	2012 Nov 28	2120	M2.2	S12W56	3044	0.03893	19.23	0.0007241	7.00	12.86	1.35	0.17
264	2013 Jan 11	0843	M1.2	N05E42	1180	0.00542	7.63	0.0003004	7.00	7.66	1.10	0.00
266	2013 Jan 13	0045	M1.0	N18W15	764	0.01716	7.39	0.0011418	6.06	6.18	2.70	31.98
268	2013 Feb 17	1545	M1.9	N12E23	620	0.01225	8.89	0.0000633	8.87	4.87	3.26	2.45
271	2013 Mar 21	2142	M1.6	N09W88	3516	0.03346	12.18	0.0000383	8.23	12.28	1.34	0.12
273	2013 Apr 11	0655	M6.5	N11E13	1076	0.04168	11.42	0.0018528	5.27	25.55	0.50	0.91
274	2013 Apr 12	1952	M3.3	N21W47	2012	0.02328	18.80	0.0013568	7.29	13.87	0.93	0.18
276	2013 May 2	0458	M1.1	N10W19	2380	0.00017	19.42	0.0007521	4.69	8.24	0.17	0.00
277	2013 May 3	1639	M1.3	N11W38	2872	0.00010	18.37	0.0009633	5.20	3.04	0.59	0.37
278	2013 May 3	1724	M5.7	N15E83	1316	0.03689	22.67	0.0033001	6.85	13.27	1.26	0.07
283	2013 May 12	2237	M1.2	N10E89	1872	0.00186	20.36	0.0014919	6.05	11.68	0.34	0.15
284	2013 May 13	0153	X1.7	N11E89	2496	0.10615	12.49	0.0132431	7.65	16.33	1.56	0.11
285	2013 May 13	1157	M1.3	N10E89	1048	0.00403	23.26	0.0014927	6.72	3.52	3.04	0.00
288	2013 May 15	0125	X1.2	N10E68	3524	0.09999	11.15	0.0031250	8.06	22.63	0.93	0.83
289	2013 May 16	2136	M1.3	N11E40	1280	0.00133	20.44	0.0000784	8.12	7.27	0.59	0.15
291	2013 May 20	0516	M1.7	N09E89	1380	0.01296	12.50	0.0000855	8.06	8.08	1.57	1.98
292	2013 May 22	1308	M5.0	N14W87	3248	0.04485	11.64	0.0011678	4.63	20.27	0.73	0.18
293	2013 May 31	1952	M1.0	N12E42	1060	0.00112	11.25	0.0000235	8.27	9.35	0.37	0.06
297	2013 Jun 23	2048	M2.9	S18E63	1132	0.02889	6.25	0.0007958	7.29	5.01	4.79	0.06
298	2013 Jul 03	0700	M1.5	S14E82	1548	0.01205	22.27	0.0000406	8.91	9.38	1.21	0.13
299	2013 Aug 12	1021	M1.5	S21E17	1536	0.00450	12.44	0.0000636	8.64	11.58	0.54	1.24
303	2013 Oct 11	0701	M1.5	N21E87	1124	0.01884	17.17	0.0002881	5.13	3.48	6.69	0.64

Table 2
(Continued)

ID	Date	Time	*GOES* Class	Heliogr. Position	Dur. Flare $\tau_{\rm flare}$ (s)	Emission Measure EM_{49} (cm^{-3})	Temp. Max. T_e (MK)	Photon Flux I_1 (cm^2 s keV^{-1})	Spectral Slope γ	Length Scale L (Mm)	Density Maximum n_{10} (cm^{-3})	Density Preflare b_{10} (cm^{-3})
304	2013 Oct 13	0012	M1.7	S22E17	1416	0.67760	11.05	0.0001016	6.80	9.52	8.86	2.12
307	2013 Oct 17	1509	M1.2	S09W63	1696	0.00352	11.69	0.0000092	9.04	10.42	0.56	0.07
308	2013 Oct 22	0014	M1.0	N08E20	1068	0.00014	21.27	0.0003649	6.90	8.32	0.15	0.00
311	2013 Oct 23	2041	M2.7	N08W06	3368	0.01733	18.16	0.0008089	6.76	9.50	1.42	3.60
312	2013 Oct 23	2333	M1.4	N09W08	2000	0.01171	15.02	0.0001602	5.42	6.49	2.07	0.24
313	2013 Oct 23	2358	M3.1	N09W09	452	0.00031	21.46	0.0003714	7.34	8.84	0.21	0.00
317	2013 Oct 25	0248	M2.9	S07E76	3164	0.03163	18.68	0.0004501	7.18	12.85	1.22	0.94
318	2013 Oct 25	0753	X1.7	S08E73	676	0.04461	33.74	0.0298859	7.58	11.36	1.74	0.17
320	2013 Oct 25	1451	X2.1	S06E69	3568	0.10233	11.35	0.0003450	10.39	16.98	1.45	0.54
321	2013 Oct 25	1702	M1.3	S08E67	2052	0.01089	15.70	0.0008598	5.99	7.14	1.73	1.22
325	2013 Oct 26	0917	M1.5	S08E59	1060	0.00078	11.77	0.0001197	6.67	6.48	0.54	0.08
328	2013 Oct 26	1949	M1.0	S08E51	1940	0.00004	20.02	0.0001241	6.61	3.87	0.25	0.00
334	2013 Oct 28	1446	M2.7	S08E27	2600	0.00557	19.67	0.0006088	7.57	23.10	0.21	0.07
336	2013 Oct 28	2048	M1.5	N07W83	1748	0.00481	8.04	0.0002001	7.99	6.48	1.33	1.22
340	2013 Nov 2	2213	M1.6	S12W12	768	0.00239	8.99	0.0002536	7.73	5.47	1.21	0.19
343	2013 Nov 5	1808	M1.0	S12E47	1124	0.00159	6.43	0.0001669	7.77	4.57	1.29	5.16
345	2013 Nov 6	1339	M3.8	S09E35	1936	0.00399	9.70	0.0031537	6.63	7.92	0.90	0.15
347	2013 Nov 7	0334	M2.3	S08E26	1436	0.02208	3.12	0.0064472	5.08	12.92	1.01	0.04
351	2013 Nov 10	0508	X1.1	S11W17	3284	0.04878	21.66	0.0079130	7.69	22.03	0.68	0.20
352	2013 Nov 11	1101	M2.4	S17E74	3068	0.00399	19.31	0.0002777	7.71	10.35	0.60	0.10
353	2013 Nov 13	1457	M1.4	S20E46	1400	0.00130	20.16	0.0001988	7.48	14.63	0.20	0.07
354	2013 Nov 15	0220	M1.0	N07E53	1252	0.00109	20.12	0.0001849	7.62	9.28	0.37	0.03
357	2013 Nov 17	0506	M1.0	S19W41	1208	0.00089	6.36	0.0002105	7.49	2.98	1.84	0.46
359	2013 Nov 21	1052	M1.2	S14W89	1248	0.02074	16.89	0.0004123	4.71	4.55	4.69	2.51
360	2013 Nov 23	0220	M1.1	N13W58	2584	0.00110	17.26	0.0000888	7.99	5.71	0.77	0.25
363	2013 Dec 19	2306	M3.5	S16E89	2304	0.01275	21.85	0.0004127	8.06	15.14	0.61	0.04
364	2013 Dec 20	1135	M1.6	S16E78	4272	0.00332	15.97	0.0001171	6.64	7.27	0.93	0.58
365	2013 Dec 22	0805	M1.9	S17W51	1788	0.00701	18.95	0.0003829	7.68	5.42	2.10	0.25
366	2013 Dec 22	0833	M1.1	S17W52	1956	0.00852	15.06	0.0004831	4.45	6.18	1.90	0.28
367	2013 Dec 22	1424	M1.6	S16E44	2532	0.03249	11.35	0.0004446	6.57	9.85	1.84	0.06
368	2013 Dec 22	1506	M3.3	S17W55	1328	0.00742	21.78	0.0003082	7.26	13.71	0.54	0.37
377	2014 Jan 3	1241	M1.0	S04E52	1000	0.02158	7.58	0.0004308	4.84	3.83	6.20	2.66
382	2014 Jan 7	0349	M1.0	N07E07	1432	0.00661	7.25	0.0007455	6.14	4.20	2.99	0.39
385	2014 Jan 8	0339	M3.6	N11W88	2016	0.01548	19.24	0.0020340	6.89	3.83	5.25	0.52
386	2014 Jan 13	2148	M1.3	S08W75	660	0.00086	7.92	0.0019242	6.65	2.97	1.81	0.39
387	2014 Jan 27	0105	M1.0	S16E88	2860	0.00172	16.77	0.0002649	4.60	11.25	0.35	0.03
389	2014 Jan 27	2205	M4.9	S14E88	1880	0.00078	24.20	0.0041016	6.96	4.85	0.83	61.62
393	2014 Jan 28	1233	M1.3	S15E79	1708	0.00363	5.90	0.0000335	8.80	4.85	1.78	0.00
395	2014 Jan 28	2204	M2.6	S14E74	1112	0.00399	7.01	0.0021642	6.82	5.69	1.47	0.79

Note. Table 2 is published in machine-readable format. The machine-readable version includes all the data from Table 3.

(This table is available in its entirety in machine-readable form.)

of the previous results is that the nonthermal energy $E_{\rm th}$ as a fraction of the dissipated magnetic free energy $E_{\rm diss}$ is $q_E = E_{\rm nth}/E_{\rm diss} = 0.51 \pm 0.17$, so about half of the dissipated magnetic energy is converted into acceleration of electrons (Aschwanden et al. 2017). If we plot the same ratios for each of the theoretical models, we find $q_E^{\rm ne} = 0.40 \pm 0.10$ for the electron number model (Figure 6(a)), $q_E^{\rm wt} = 0.45 \pm 0.10$ for the warm target model (Figure 6(b)), $q_E^{\rm tof} = 0.58 \pm 0.16$ for the time-of-flight model (Figure 6(c)), and $q_E^{\rm co} = 0.0034 \pm 0.0006$ for the cross-over model (Figure 6(d)).

Since the three methods of calculating the nonthermal energy are essentially independent, we can improve the accuracy of the statistical means by averaging (logarithmically) the values from two or three models; this is shown in Figure 7. Combining the electron number and the warm target models we find $q_E^{\rm ne,wt} = 0.57 \pm 0.10$ (Figure 7(a)), combining the electron number and the time-of-flight models we find $q_E^{\rm ne,tof} = 0.52 \pm 0.09$ (Figure 7(b)), and by combining the warm target and the time-of-flight models we find $q_e^{\rm wt,tof} = 0.61 \pm 0.10$ (Figure 7(c)). The largest statistics is achieved by combining all three methods (excluding the cross-over model), for which we find $q_e^{\rm en,wt,tof} = 0.57 \pm 0.08$ (Figure 7(d)), which is perfectly consistent with the earlier result of $q_E = 0.51 \pm 0.17$ (Aschwanden et al. 2017). However, the new result has a smaller error of the mean ($q_{\rm err} = \pm\, 0.07$) than the old result ($q_{\rm err} = \pm\, 0.17$), thanks to the larger statistics with multiple independent methods, which cancel out some of the systematic errors of the various models. Note that the uncertainty of the ratio of the nonthermal to the dissipated magnetic energy, i.e., $q_E = E_{\rm diss}/E_{\rm magn}$, has been reduced to a factor of $\sigma \approx 5$ for a

Table 3
Low-energy Cutoff Energies and Total Nonthermal Energies Calculated for Four Models, Derived from the Observables of 143 M- and X-class Flare Events Given in Table 2

ID	Cutoff Energy ε_{en} (keV)	Cutoff Energy ε_{wt} (keV)	Cutoff Energy ε_{tof} (keV)	Cutoff Energy ε_{co} (keV)	Nonthermal Energy E_{en} (10^{30} erg)	Nonthermal Energy E_{wt} (10^{30} erg)	Nonthermal Energy E_{tof} (10^{30} erg)	Nonthermal Energy E_{co} (10^{30} erg)
1	1.00	4.80	6.70	15.00	0.7778	0.0042	0.0015	0.0001
2	3.20	6.60	1.70	19.00	0.0305	0.0017	0.4079	0.0000
3	0.70	5.30	1.90	30.00	21.5602	0.0497	1.2021	0.0002
4	11.50	14.20	11.20	21.00	2.2251	0.4854	2.6257	0.0307
10	16.20	13.40	9.00	30.00	1.4205	4.5095	49.6561	0.0333
12	12.80	14.80	15.10	27.00	46.3275	19.9327	17.1499	0.5138
13	8.70	12.60	5.90	21.00	2.4624	0.2781	23.6050	0.0143
15	9.20	8.90	9.90	22.00	5.1154	6.0449	3.1357	0.0165
16	14.90	6.90	15.50	27.00	2.5982	312.6780	2.0072	0.0636
18	10.50	9.60	10.90	24.00	0.8962	1.6026	0.7330	0.0057
19	1.90	3.20	9.70	15.00	0.3648	0.0681	0.0017	0.0004
20	10.70	5.80	10.40	22.00	2.0033	143.3275	2.4943	0.0132
21	9.90	9.60	7.50	15.00	5.4652	7.0165	52.4010	0.1755
22	7.60	5.50	5.30	22.00	5.5665	35.2264	41.2397	0.0164
23	9.80	5.80	6.40	20.00	3.4690	90.9612	49.9326	0.0367
28	5.40	5.60	4.50	15.00	6.6379	5.5572	14.3126	0.0957
29	12.90	6.00	5.20	26.00	0.1107	4.2193	8.2575	0.0039
30	9.20	2.70	9.60	22.00	0.9000	895.5553	0.7023	0.0063
31	7.90	4.50	38.30	30.00	16.7310	975.3401	0.0002	0.0012
33	29.20	16.20	6.60	21.00	0.0294	1.3916	495.0242	0.2530
34	6.10	7.70	5.80	15.00	416.3836	68.0520	624.6119	0.2839
37	12.80	8.40	9.30	28.00	5.1082	41.4942	25.9488	0.0969
38	10.00	5.70	11.80	20.00	0.6242	26.0680	0.2079	0.0063
40	11.30	7.40	18.20	30.00	3.8600	47.7786	0.2403	0.0126
41	4.10	4.70	13.20	15.00	1.1429	0.6713	0.0102	0.0060
46	8.80	8.20	7.90	20.00	7.1019	10.9290	13.8560	0.0568
48	96.70	8.20	8.80	16.00	0.0000	5.1251	3.4567	0.0888
50	2.00	3.10	35.60	12.00	2.7037	0.6692	0.0005	0.0127
51	6.60	7.90	6.50	12.00	14.6050	4.8811	16.0264	0.3311
52	8.10	9.80	6.40	15.00	10.3822	2.4438	71.7504	0.0802
53	14.20	13.00	21.20	15.00	5.3108	9.4608	0.3361	3.6127
55	54.60	9.60	7.70	19.00	0.0001	5.8205	24.7286	0.0624
61	14.50	18.60	13.90	28.00	106.4098	21.3920	137.7906	1.5931
63	10.40	11.30	5.10	18.00	1.3532	0.7893	198.1350	0.0300
64	8.10	11.30	7.10	30.00	2.6708	0.2223	6.7030	0.0002
65	12.00	8.10	9.30	30.00	22.9111	404.4191	152.0502	0.0251
68	10.50	16.70	14.30	18.00	101.2172	3.2939	10.3612	1.9095
69	10.50	6.70	9.60	16.00	9.9118	168.5142	17.3350	0.7104
70	7.60	10.80	6.60	17.00	19.8497	1.0888	68.6569	0.0234
71	21.20	16.10	4.80	30.00	0.0204	0.1367	570.6394	0.0019
77	9.00	7.50	6.00	15.00	3.5533	11.7135	50.8674	0.1313
81	13.40	6.90	11.00	23.00	0.7741	59.5029	2.8106	0.0225
83	6.30	6.60	8.00	14.00	98.3267	65.8536	19.0484	0.4112
84	8.60	5.70	14.90	29.00	6.2511	51.7382	0.4210	0.0151
86	8.80	10.20	5.80	28.00	1.7223	0.6667	31.8594	0.0007
91	7.00	7.20	8.30	12.00	135.1171	107.9637	37.2981	2.0702
98	15.90	9.70	8.70	20.00	1.0634	39.2940	82.8666	0.2042
100	14.90	14.90	8.40	20.00	0.6826	0.7121	38.6946	0.0894
101	11.20	4.90	11.70	15.00	0.0898	13.9602	0.0692	0.0157
103	12.80	13.70	10.50	28.00	0.9179	0.5842	2.9818	0.0077
111	10.30	13.20	4.90	22.00	1.4515	0.2686	201.8147	0.0086
116	23.70	7.10	5.80	14.00	0.0077	47.6822	205.9947	0.3427
120	7.70	5.80	9.50	15.00	6.5091	44.8960	1.4804	0.0639
122	10.00	12.00	7.40	27.00	2.4833	0.6709	21.1648	0.0022
123	9.90	11.50	5.80	28.00	4.1542	1.4337	172.7290	0.0031
125	8.20	14.50	7.30	26.00	6.0413	0.1924	11.8059	0.0056
126	8.40	11.00	6.40	22.00	13.1490	1.9445	99.5300	0.0130
157	36.50	9.50	7.40	14.00	0.0001	3.0211	21.6221	0.1610
158	5.30	7.60	7.40	15.00	1.3581	0.2412	0.2706	0.0095
159	7.30	11.50	12.30	17.00	7.0812	0.5296	0.3739	0.0578
160	5.90	2.10	12.70	17.00	3.0419	473.1884	0.0663	0.0157

Table 3
(Continued)

ID	Cutoff Energy ε_{en} (keV)	Cutoff Energy ε_{wt} (keV)	Cutoff Energy ε_{tof} (keV)	Cutoff Energy ε_{co} (keV)	Nonthermal Energy E_{en} (10^{30} erg)	Nonthermal Energy E_{wt} (10^{30} erg)	Nonthermal Energy E_{tof} (10^{30} erg)	Nonthermal Energy E_{co} (10^{30} erg)
167	0.40	4.60	8.60	21.00	30.2518	0.0892	0.0196	0.0022
168	9.70	8.30	6.50	15.00	1.7269	4.1018	15.3409	0.1610
169	6.60	8.60	11.00	15.00	110.4820	16.9623	3.0718	0.3498
170	0.70	1.60	13.00	14.00	19.2109	1.2400	0.0019	0.0015
173	13.90	6.10	10.20	20.00	0.4422	140.1815	3.7789	0.0338
176	2.90	5.10	12.80	15.00	0.5684	0.0932	0.0047	0.0028
178	9.10	7.90	12.50	19.00	1.6227	3.9857	0.1907	0.0118
182	7.30	9.30	6.60	30.00	10.8205	2.1517	21.4655	0.0008
187	11.40	9.40	11.40	22.00	10.0191	33.7559	10.0593	0.1921
189	0.60	4.50	12.30	16.00	0.6845	0.0060	0.0006	0.0003
190	0.10	3.90	8.00	14.00	4.6077	0.0036	0.0010	0.0004
195	12.80	6.80	12.40	24.00	4.9962	219.9091	5.9444	0.1149
196	9.30	8.60	6.80	22.00	3.5504	6.0006	25.6911	0.0142
199	6.30	7.50	9.70	18.00	5.3694	2.2979	0.6250	0.0267
200	1.00	8.20	1.80	15.00	40.7531	0.0202	5.0761	0.0024
203	14.50	10.00	11.40	21.00	0.4537	6.5307	2.5106	0.0320
205	5.70	8.30	10.80	22.00	5.8572	0.9418	0.2667	0.0089
208	8.60	10.00	7.60	24.00	6.2984	2.6349	14.0258	0.0131
210	11.70	12.80	8.10	24.00	0.4536	0.2598	4.1385	0.0062
211	5.90	10.30	6.90	30.00	2.0414	0.0798	0.8681	0.0001
212	4.90	15.30	9.90	24.00	505.2834	0.4216	6.1786	0.0257
214	19.60	12.80	6.10	30.00	0.0259	0.5373	105.4782	0.0012
215	5.70	8.90	11.40	17.00	8.9478	0.8496	0.2419	0.0290
219	9.30	13.00	6.00	30.00	7.8497	0.9755	110.5648	0.0055
223	14.80	7.50	14.20	16.00	0.7552	30.5329	0.9672	0.5032
228	5.40	3.40	16.20	15.00	0.7626	5.0530	0.0073	0.0101
230	11.90	13.00	16.40	18.00	0.7520	0.4090	0.0897	0.0480
235	9.40	10.30	6.00	30.00	2.7705	1.4368	84.1892	0.0005
238	8.30	19.90	10.30	17.00	26.7858	0.0172	4.5569	0.0661
241	7.60	6.60	7.30	16.00	9.4226	23.5095	11.6637	0.0967
245	15.90	8.30	15.10	20.00	2.5768	276.5678	3.7736	0.5087
246	11.40	14.30	9.00	22.00	1.3530	0.3115	5.9178	0.0188
248	194.30	18.20	9.80	30.00	0.0000	0.9979	37.5929	0.0524
251	10.00	6.60	12.40	22.00	5.8906	121.1315	1.2253	0.0201
253	9.40	16.70	11.60	20.00	10.7416	0.1714	2.3528	0.0474
255	0.80	2.60	13.90	14.00	0.1509	0.0085	0.0001	0.0001
257	3.20	4.00	13.30	16.00	0.9894	0.3824	0.0035	0.0017
258	7.70	5.70	10.60	17.00	3.0739	14.6470	0.5495	0.0434
261	11.90	11.50	9.00	24.00	0.6241	0.8022	4.5538	0.0047
262	9.70	13.30	11.70	17.00	2.8245	0.4292	0.9263	0.0964
264	32.10	5.30	8.10	18.00	0.0016	80.4219	6.0352	0.0504
266	3.60	4.50	11.40	15.00	24.2342	8.1539	0.0734	0.0184
268	9.70	7.60	11.10	30.00	2.4258	17.6247	0.8419	0.0003
271	9.90	9.70	11.40	14.00	3.0094	3.6091	1.1474	0.2522
273	2.30	6.20	10.00	12.00	83.7943	1.2304	0.1574	0.0719
274	10.40	13.40	10.10	16.00	13.3241	2.7140	16.7779	0.9044
276	52.20	9.50	3.30	16.00	0.0001	0.0280	1.3581	0.0041
277	9.50	9.80	3.70	21.00	0.1121	0.0971	5.6071	0.0040
278	11.60	15.30	11.40	20.00	3.1159	0.5936	3.3443	0.1256
283	7.80	12.40	5.60	29.00	1.1321	0.1071	5.9789	0.0014
284	15.80	9.30	14.10	25.00	14.9141	511.5092	32.2520	0.7191
285	77.60	15.50	9.10	28.00	0.0000	0.1121	2.2906	0.0038
288	10.30	8.70	12.80	18.00	70.1435	233.2775	15.2921	1.3882
289	11.10	16.10	5.80	30.00	1.2008	0.0851	122.8816	0.0010
291	7.80	9.80	9.90	15.00	10.7964	2.1221	1.8687	0.1025
292	2.60	5.60	10.80	14.00	8.6450	0.5070	0.0486	0.0188
293	9.80	9.00	5.20	24.00	0.6634	1.2131	65.5062	0.0010
297	15.80	4.50	13.70	15.00	0.1384	394.0855	0.3433	0.1936
298	11.60	19.00	9.40	16.00	1.5009	0.0292	7.6938	0.1153
299	8.20	10.30	7.00	15.00	15.9317	2.7585	56.0776	0.1611
303	5.00	9.10	13.50	17.00	0.2404	0.0207	0.0040	0.0016

Table 3
(Continued)

ID	Cutoff Energy ε_{en} (keV)	Cutoff Energy ε_{wt} (keV)	Cutoff Energy ε_{tof} (keV)	Cutoff Energy ε_{co} (keV)	Nonthermal Energy E_{en} (10^{30} erg)	Nonthermal Energy E_{wt} (10^{30} erg)	Nonthermal Energy E_{tof} (10^{30} erg)	Nonthermal Energy E_{co} (10^{30} erg)
304	4.80	7.40	25.70	30.00	8.2187	0.6604	0.0005	0.0002
307	10.50	10.10	6.70	23.00	2.4395	3.3935	89.3478	0.0046
308	39.30	14.50	3.20	30.00	0.0002	0.0829	654.5867	0.0011
311	6.80	12.20	10.30	21.00	21.6912	0.7447	1.9624	0.0318
312	5.00	8.30	10.20	21.00	0.1779	0.0181	0.0072	0.0003
313	20.70	15.40	3.80	30.00	0.0136	0.0883	606.1953	0.0013
317	7.60	13.20	11.10	20.00	20.5291	0.6779	1.9889	0.0513
318	16.00	25.00	12.40	30.00	10.2022	0.5564	54.3011	0.1656
320	14.60	11.10	13.80	30.00	14.5203	178.0020	23.1600	0.0163
321	6.30	9.50	9.80	16.00	1.8441	0.2419	0.2003	0.0176
325	8.70	7.80	5.20	20.00	0.5292	1.0053	9.8712	0.0048
328	26.10	13.10	2.70	30.00	0.0003	0.0150	97.9885	0.0001
334	9.70	14.50	6.20	21.00	4.4813	0.3091	84.4325	0.0276
336	10.00	6.20	8.20	17.00	2.2796	64.5426	9.3836	0.0578
340	11.80	6.80	7.20	17.00	0.7679	32.6484	21.8765	0.0662
343	8.30	4.90	6.80	21.00	3.3767	129.3156	13.4555	0.0064
345	12.80	6.40	7.40	21.00	1.1343	57.4849	24.0198	0.0702
347	7.40	1.60	10.10	14.00	0.7488	361.8527	0.2138	0.0565
351	12.80	16.20	10.80	20.00	10.7767	2.1711	33.3844	0.5354
352	12.10	14.50	7.00	23.00	2.4294	0.7171	98.3107	0.0324
353	9.00	14.70	4.80	27.00	4.3452	0.1747	244.4080	0.0035
354	12.20	15.00	5.20	26.00	0.5077	0.1293	145.9955	0.0033
357	13.10	4.70	6.50	15.00	0.1348	109.7154	12.1532	0.0556
359	2.70	8.30	12.90	15.00	2.9134	0.0436	0.0085	0.0049
360	12.20	13.40	5.90	15.00	1.2240	0.6325	201.4743	0.2834
363	12.70	17.10	8.50	21.00	2.8401	0.3577	50.4921	0.0826
364	7.40	10.50	7.30	17.00	1.8018	0.2566	2.0618	0.0171
365	13.30	14.20	9.40	22.00	0.3626	0.2367	3.6241	0.0126
366	3.30	7.10	9.60	15.00	0.1169	0.0084	0.0030	0.0006
367	10.10	7.40	11.90	14.00	0.7798	4.3741	0.3099	0.1260
368	7.30	15.50	7.60	22.00	7.7331	0.0665	5.8546	0.0074
377	3.10	3.80	13.60	16.00	0.6630	0.3083	0.0023	0.0013
382	9.70	4.50	9.90	17.00	0.1497	7.9724	0.1325	0.0082
385	14.80	13.10	12.50	16.00	0.4465	0.9144	1.1817	0.2800
386	13.70	5.20	6.50	15.00	0.1604	36.7204	10.8544	0.0947
387	3.80	8.10	5.50	15.00	0.3818	0.0258	0.1018	0.0028
389	7.50	16.60	5.60	30.00	39.5556	0.3435	224.5840	0.0101
393	25.90	5.00	8.20	30.00	0.0023	900.0698	18.1551	0.0007
395	10.60	4.70	8.10	18.00	3.1501	350.3838	15.3367	0.1457

single flare event (Figure 7(d)), while the error of the mean has been reduced to $q_{err} = 0.08$ (Figure 7(d)).

4. Discussion

4.1. Constraints for Low-energy Cutoffs

We applied four different theoretical considerations in order to determine low-energy cutoffs in hard X-ray spectra, which are useful to pinpoint systematic errors of the models. Let us discuss which parameters constrain the various models, and whether the four models have some common physics.

In the electron number model (Section 2.1) we make the assumption that all electrons in the diffusion region of a magnetic reconnection volume are accelerated out of the thermal distribution, and therefore the flare volume $V = L^3$, the preflare electron density n_e, and the flare duration τ_{flare} are needed, as well as the observables that characterize the nonthermal spectrum (I_1, ϵ_1, γ). This method therefore requires imaging observations (to measure the flare area $A = L^2$) and time profiles of the photon flux $F(t)$ (to measure the flare duration), while fewer physical parameters are required in the other models, and thus the electron number model provides the strongest constraints on the low-energy cutoff.

In the time-of-flight model (Section 2.2) we assume an equivalence between collisional deflection and electron time-of-flight times, which depend on the kinetic energy of electrons and the electron density, plus the spatial scale of the electron time-of-flight distance L_{tof}. Hence imaging observations are required also, but the low-energy cutoff depends on L_{tof} and n_e only, which amounts to fewer constraints than the electron number model.

In the simplified approximation of the warm target model (Section 2.3), only the temperature T_e is required to characterize the collisional loss in the thick-target model (besides the spectral observable γ), which is based on the same physical process of collisional thermalization as the time-of-flight model, but requires fewer physical parameters.

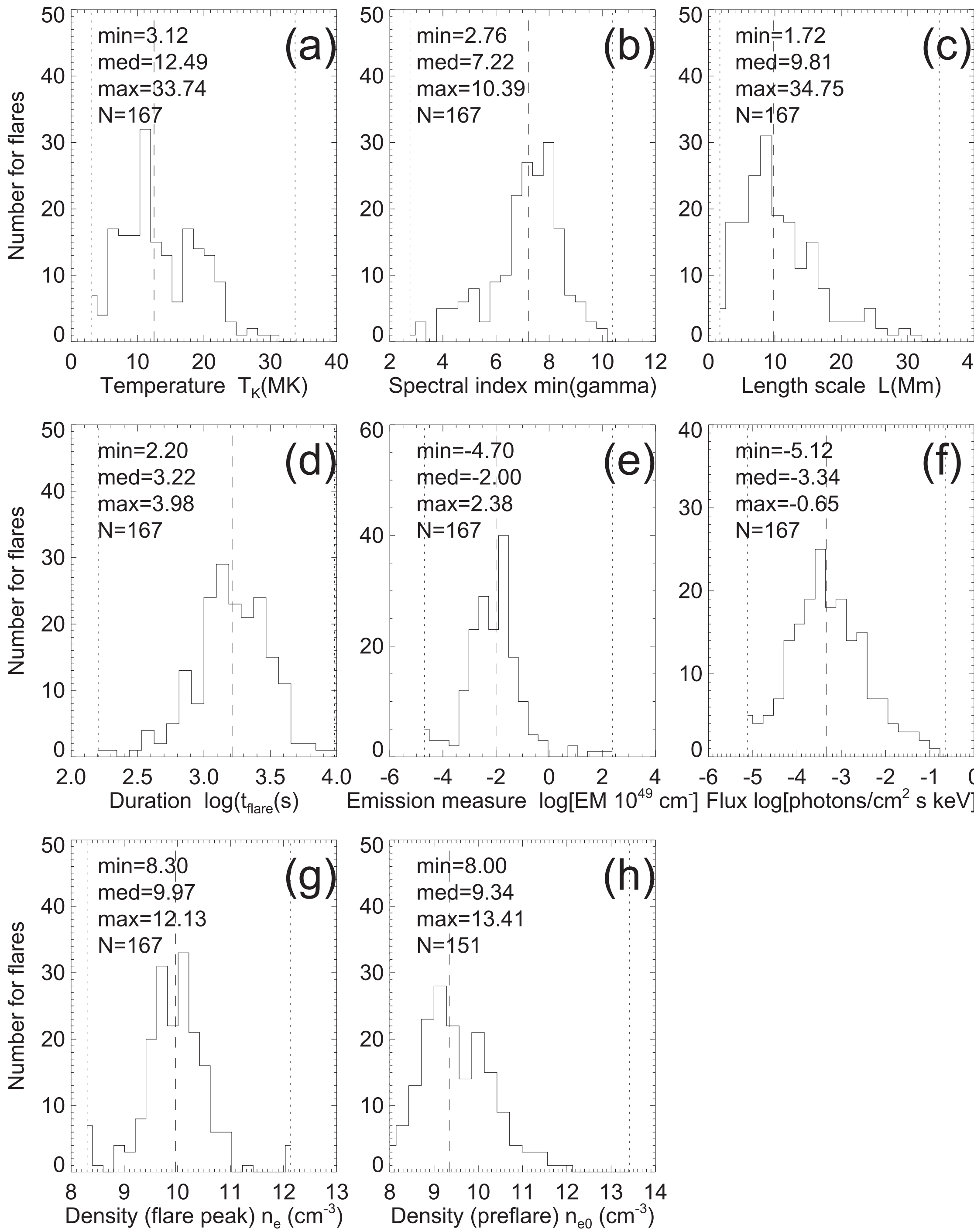

Figure 3. Distributions of measured observables required for modeling the low-energy cutoff of hard X-ray spectra of M- and X-class flares. The minimum, maximum, and median values are indicated.

Finally, in the spectral cross-over model (Section 2.4), the low-energy cutoff is directly estimated from the cross-over of the thermal and nonthermal spectrum, which does not require the knowledge of any physical parameter. However, this simplest method provides upper limits on the low-energy cutoff only.

So, the four methods are all complementary and at this point we cannot claim which model has a systematically higher value for the calculation of the low-energy cutoff, except for the fourth method, which provides upper limits on the low-energy cutoff only. How compatible are the different models? For the scaling of the physical parameters L and n_e in the two first models, we find $\varepsilon_{\rm en} \propto (n_e L^3)^{-1/\gamma}$ for the electron number model (Equation (9)), and $\varepsilon_{\rm tof} \propto (n_e L)^{1/2}$ for the time-of-flight model (Equation (20)), which are not directly compatible, and thus indicate incomplete physical models.

4.2. Functional Shape of the Low-energy Cutoff

In most previous, work the functional shape of the (nonthermal) electron injection spectrum is characterized with a power-law function, i.e., $f(\varepsilon \geqslant \varepsilon_c) \propto \varepsilon^{-\delta}$, with a sharp

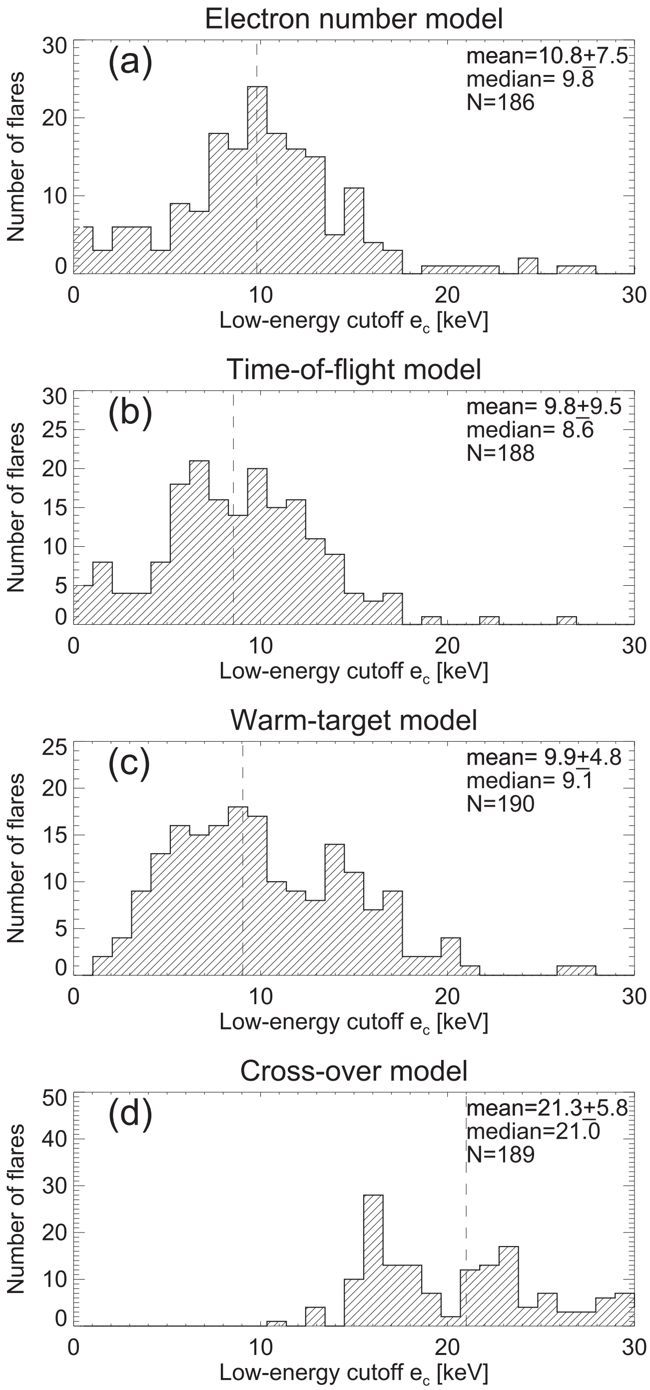

Figure 4. Distribution of low-energy cutoffs in (a) the electron number model, (b) the time-of-flight model, (c) the warm target model, and (d) the cross-over model. Note that the first three models all yield a low-energy cutoff energy of $e_c \approx 10$ keV, while the cross-over model predicts upper limits only, at $e_c \approx 21$ keV.

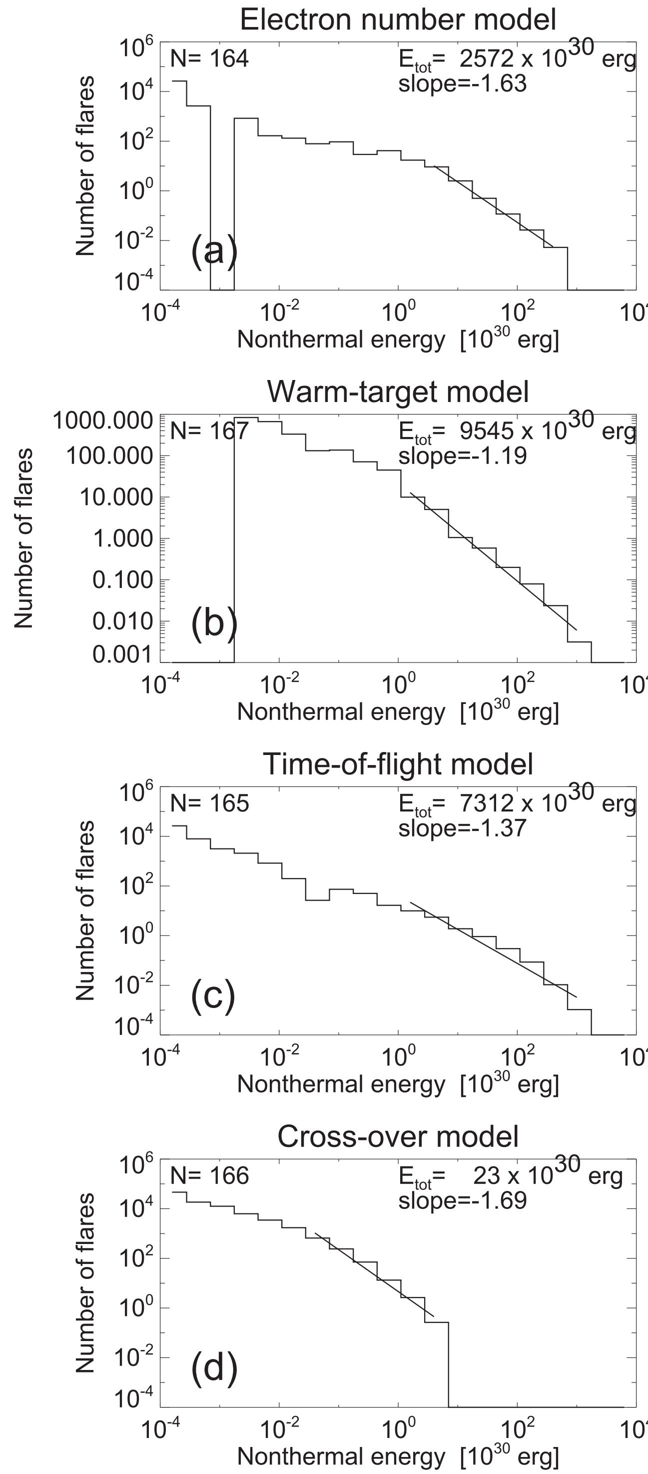

Figure 5. Size distributions of nonthermal energies $E_{\rm nth}$ (histograms with power-law fits) and total nonthermal energy $E_{\rm tot}$ contained in each distribution for the four different models of the low-energy cutoff e_c.

cutoff at the low-energy side of the spectrum. This functional choice of the spectrum is not constrained by any physical model, but is simply chosen for mathematical convenience. The steep fall-off of this function at $\varepsilon \geqslant \varepsilon_c$ creates a particle energy distribution peaking near ε_c, which is unlikely to occur in a collisional plasma. We can use a kappa-distribution instead, already implemented in OSPEX. There are very few studies of the low-energy cutoff with smooth functions, such as modeling with kappa-distributions (Bian et al. 2014; Kontar et al. 2019).

Alternatively, we derive a smooth low-energy cutoff function in Appendix A, which is not based on a physical model either, but represents the simplest spectral function with a low-energy cutoff at the lower end and a power-law function at the upper end (Equation (41)). We show an example in Figure 8, where the smooth low-energy cutoff function (according to Equation (41)) is shown with a minimum energy of $\varepsilon_c = 10.0$ keV, a power-law slope of $\delta = 3$, and a peak

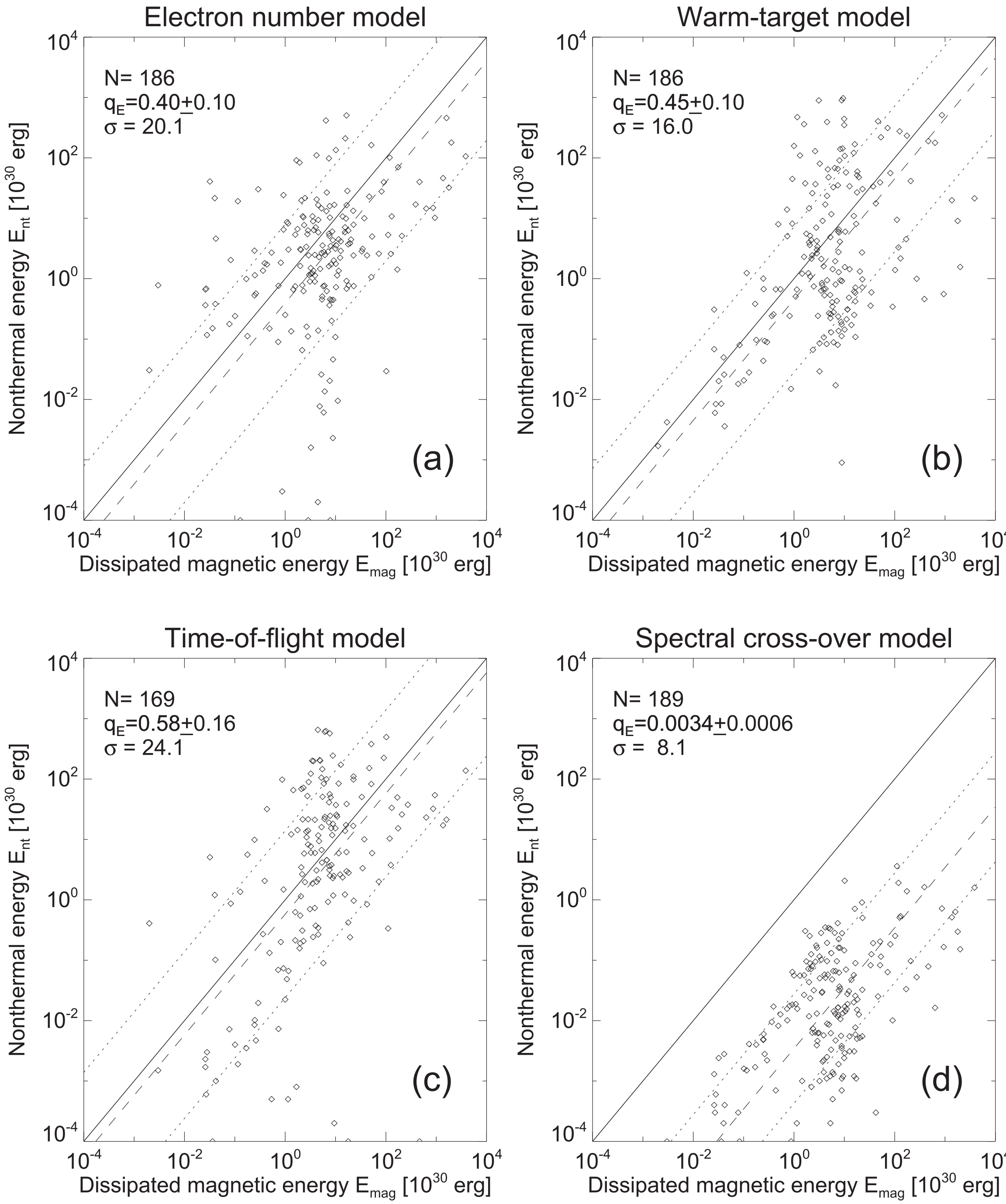

Figure 6. Scatterplots of nonthermal energy in accelerated electrons ($E_{\rm nth}$) as a function of the dissipated magnetic energy ($E_{\rm diss}$). Equivalence is rendered with a solid diagonal line, the logarithmically averaged ratios (q_E) with a dashed line, and the standard deviation factors (σ) with dotted lines.

energy of $\varepsilon_{\rm peak} = \varepsilon_{\rm min}\ (1 + 1/\delta) = 13.3$ keV. Although the difference in the sharp and the smooth electron injection spectrum does not appear to be paramount on a log–log scale (Figure 8, left), the same functions rendered on a linear scale (Figure 8, right) clearly show a significant difference in the electron flux. The suitability of a smooth cutoff function would require a spectral fit in the 10–30 keV range for this particular example. This example illustrates that the electron flux or the nonthermal energy calculated with a smooth cutoff function would yield a significantly different value than the sharp cutoff function. Smooth functions appear to be more realistic in a collisional plasma than an infinitely sharp edge at the low-energy cutoff.

4.3. Uncertainties of Nonthermal Energies in Flares

A central question of this study is the statistical uncertainty of the various forms of flare energies, in particular the nonthermal energies of flares. From the distributions of (logarithmic) nonthermal energies we found means and standard deviations of $q_E = 0.40 \pm 0.10$ for the electron number model (Figure 6(a)), $q_E = 0.58 \pm 0.16$ for the time-of-flight model (Figure 6(c)), and $q_E = 0.45 \pm 0.19$ for the

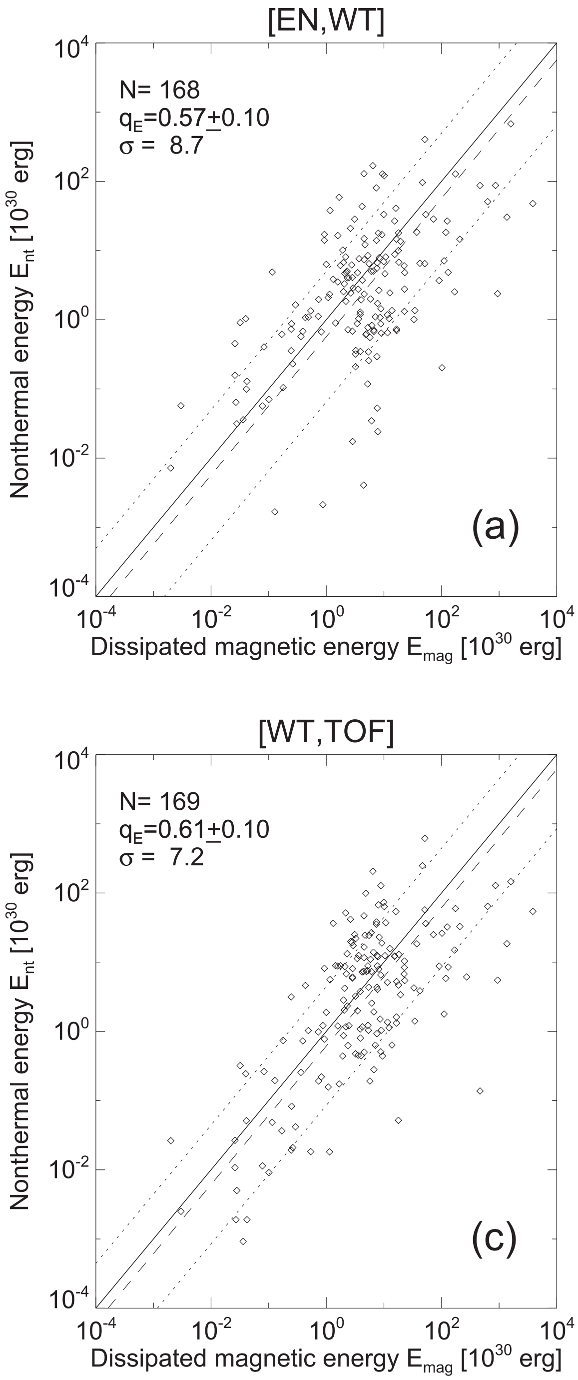

Figure 7. Scatterplots of nonthermal energy in accelerated electrons (E_{nth}) as a function of the dissipated magnetic energy (E_{diss}), averaged from two or three methods: (a) electron number/warm target, (b) electron number/time-of-flight, (c) warm target/time-of-flight, and (d) electron number/warm target/time-of-flight, with similar representation as Figure 6. Note that the logarithmically averaged ratios are compatible with the previous result of $E_{\mathrm{nth}}/E_{\mathrm{diss}} = 0.51 \pm 0.17$ (Aschwanden et al. (2017).

warm target model (Figure 6(b)), which are fully compatible with the previously measured values of $q_E = 0.51 \pm 0.17$ based on the warm target model using different temperature mixtures (Aschwanden et al. 2017). The error of the mean is even smaller when all measurements from the three methods are combined, i.e., $q_e = 0.57 \pm 0.08$ (Figure 7(d)). However, the standard deviations of the energy ratios scatter by factors of $\sigma \approx 8$–24 (Figure 6), which represent the uncertainties for single events. Combining the first three methods, the uncertainty for a single event comes down to a factor of $\sigma = 5.4$ (Figure 7(d)). Since these energy ratios $q_E = E_{\mathrm{nth}}/E_{\mathrm{diss}}$ involve both the nonthermal energies and the dissipated magnetic energies, the uncertainties of both types of energies are folded into these uncertainties. In summary, we can say that the statistical error of the mean nonthermal-to-magnetic energy ratio has been reduced to $\gtrsim 8\%$, while the uncertainty of the ratio for an individual event has been reduced to a factor of 5. Future studies should concentrate on cases with unphysical values, such as flares that yield nonthermal energies larger than the dissipated magnetic energy.

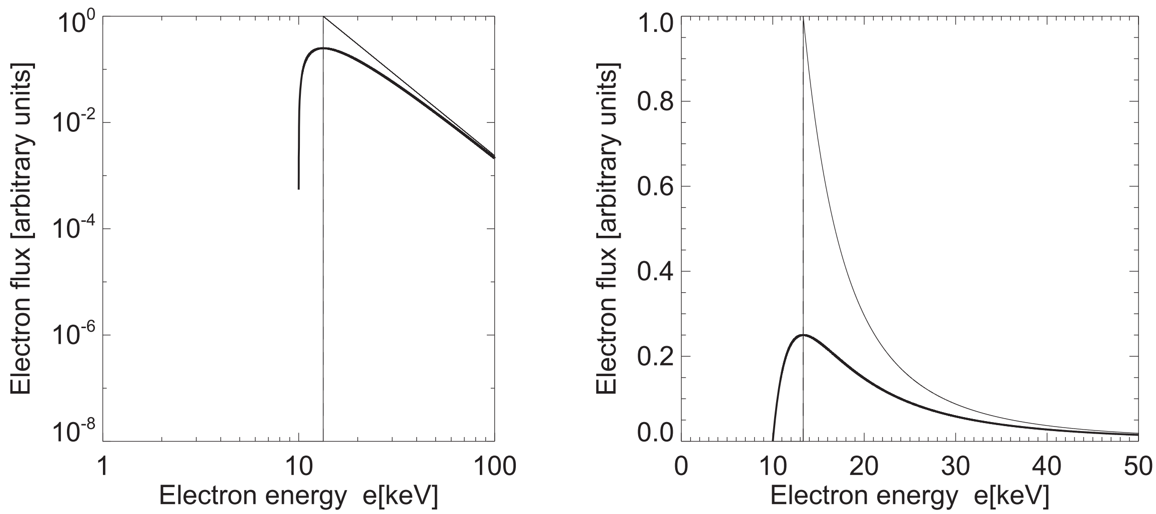

Figure 8. Electron injection spectrum with a smooth low-energy cutoff at the lower end (thick line), asymptotically approaching a power-law function at the upper end (as defined in Equation (41)), rendered on a log–log scale (left panel), as well as on a linear scale (right panel). The power-law slope of the electron injection spectrum is $\delta = 3$, the minimum energy is $\varepsilon_{\min} = 10$ keV, and the peak energy is $\varepsilon_{\rm peak} = 13.3$ keV, with ratio $\varepsilon_{\rm peak}/\varepsilon_{\min} = (1 + 1/\delta) = 4/3$.

5. Conclusions

In this study we revisit the nonthermal flare energies previously calculated for 191 flare events (M and X class) observed with *RHESSI* during 2010–2014 (Aschwanden et al. 2016), based on the warm target model of Kontar et al. (2015, 2019). The warm target model predicts a low-energy cutoff that scales linearly with temperature T_e of the warm target and spectral power-law slope δ of the nonthermal electron flux, i.e., $\varepsilon_c \approx \delta k_B T_e$ (Kontar et al. 2015). The power-law slope δ is obtained from a spectral fit of *RHESSI* data with the OSPEX software, applied to the nonthermal energy range of $\varepsilon \approx 10$–30 keV. The temperature is weighted by a mixture of preflare plasma temperatures ($T_{\rm cold}$) and heated upflowing evaporating flare plasma temperatures ($T_{\rm hot}$), which has a mean value of $T_e = 8.8 \pm 6.0$ MK for AIA data, from which the mean values of the DEM peak temperatures were used in the previous study (Aschwanden et al. 2016). These parameters yield a mean energy cutoff of $e_{\rm wt} = 6.2 \pm 1.6$ keV in the warm target model, and an energy fraction of $q_E = 0.51 \pm 0.17$ for the mean (logarithmic) ratio of the nonthermal energy to the dissipated magnetic energy.

Since the nonthermal flare energies represent the largest fraction of the total energy budget in flares, and since the determination of the nonthermal flare energy has the largest uncertainty due to the unknown low-energy cutoff, we decided to revisit the calculation of nonthermal energies with four different physical models that complement each other, which we summarize as follows.

1. The *electron number model* estimates the number of electrons (in the preflare phase) that can be accelerated in a flaring region, which is the product of the (preflare) electron density n_e, the flare volume V, and the flare duration $\tau_{\rm flare}$. Some geometric factor is required to relate the acceleration volume to the flaring volume seen in EUV. Setting this total electron number equal to the total number of electrons contained in the electron injection spectrum according to the thick-target model, a low-energy cutoff $\varepsilon_{\rm en}$ can be derived that depends on the spectral parameters [$I_1(t)$, $\gamma(t)$] and the physical parameters [n_e, V, $\tau_{\rm flare}$]. Using this model we infer a low-energy cutoff of $\varepsilon_{\rm en} = 10.8 \pm 7.5$ keV and a value of $E_{\rm nth}/E_{\rm diss} = 0.40 \pm 0.10$ for the ratio of the nonthermal to the dissipated magnetic energy.
2. The *time-of-flight* model assumes an equivalence of the collisional deflection time $t_{\rm defl}$ and the electron time-of-flight timescale $t_{\rm tof}$. This model essentially assumes a non-collisional plasma for $t_{\rm tof} < t_{\rm defl}$, and a collisional plasma for longer propagation times, $t_{\rm tof} > t_{\rm defl}$. This model predicts a low-energy cutoff that depends on the electron time-of-flight distance $L_{\rm tof}$ (which we approximate with the length scale $L_{\rm tof}$ of the flare area) and the preflare electron density n_e. Using this model we infer a low-energy cutoff of $\varepsilon_{\rm tof} = 9.8 \pm 9.5$ keV and a value of $E_{\rm nth}/E_{\rm diss} = 0.58 \pm 0.16$ for the ratio of the nonthermal to the dissipated magnetic energy.
3. The *warm target* model, derived by Kontar et al. (2015), replaces the original cold thick-target model, where in addition to the "cold" chromospheric plasma, a "warm" coronal plasma is added, where the precipitating electrons collisionally thermalize in the ambient coronal Maxwellian distribution. Importantly, the thermalized electrons contribute to the overall thermal spectrum. The "warm" temperature of the coronal plasma can be a mixture of cold and hot plasma, which we approximate here with the geometric mean of the "cold" EUV temperature (obtained from DEM modeling) and the "hot" soft X-ray plasma temperature (obtained from *RHESSI* fitting with a combined thermal plus nonthermal spectrum). Using this model we infer a low-energy cutoff of $\varepsilon_{\rm wt} = 9.9 \pm 4.8$ keV and a value of $E_{\rm nth}/E_{\rm diss} = 0.45 \pm 0.10$ for the ratio of the nonthermal to the dissipated magnetic energy.
4. The *spectral cross-over* model is included here for comparison. An upper limit for the low-energy cutoff can be found from the intersection point of the thermal (low-energy) component and the nonthermal (high-energy) component in spectral fits of *RHESSI* data, using the OSPEX software. As was established earlier, the low-energy cutoff is different by about a factor of 2, for which we find a range of $\varepsilon_{\rm co} = 21.3 \pm 5.8$ keV.

In summary, we conclude that the first three models yield consistent values for the low-energy cutoff in the order of $\varepsilon \approx 10$ keV, while the spectral cross-over model yields upper limits only, at $\varepsilon \approx 21$ keV. It is interesting that the first three different models with different assumptions lead to similar results. Combining all three methods, we find a mean energy partition of $q_E = 0.57 \pm 0.08$ for nonthermal energies, while the uncertainty in a single event has been reduced to a factor of 5.

We acknowledge useful discussions with John Raymond. This work was partially supported by NASA contracts NNX11A099G, NNG04EA00C (*SDO*/AIA), and NNG09FA40C (IRIS). E.P.K. and N.L.S.J. were supported by the Space and Technology Facilities Council (UK) ST/L000741/1.

Appendix A
Smooth Low-energy Cutoff Function

The electron injection spectrum in the thick-target model is generally rendered with a power-law function that drops off steeply above the cutoff energy at $\varepsilon \geqslant \varepsilon_c$, and is set to zero below this cutoff energy at $\varepsilon < \varepsilon_c$ (e.g., Holman 2003). This form of spectral function results in an extremely narrow function in energy that is almost mono-energetic. For collisional processes, a sharp cutoff function may be unrealistic, while a smooth cutoff function is more likely to occur. We define a smooth electron injection function $f_e(\varepsilon)$ simply by introducing a multiplicative term $(1 - \varepsilon_c/\varepsilon)$:

$$f_e^{\rm sm}(\varepsilon) = f_e(\varepsilon)\left(1 - \frac{\varepsilon_{\rm min}}{\varepsilon}\right), \qquad (41)$$

which fulfills the two constraints of a low-energy cutoff of $f_e^{\rm sm}(\varepsilon = \varepsilon_{\rm min}) = 0$ and the approximative form of a power-law-like function at higher energies, i.e., at $\varepsilon \gtrsim \varepsilon_{\rm min}$.

The smooth electron injection spectrum (as shown by a thick line in Figure 8) has then the functional form of (based on Equation (2))

$$f_e^{\rm sm}(\varepsilon) = f_1\left(\frac{\varepsilon}{\varepsilon_{\rm min}}\right)^{-\delta}\left(1 - \frac{\varepsilon_{\rm min}}{\varepsilon}\right). \qquad (42)$$

The smoothed electron injection function has a minimum energy of $\varepsilon_{\rm min}$, and a peak at $\varepsilon_{\rm peak}$. If we set the peak energy equal to the sharp cutoff, i.e., $\varepsilon_{\rm peak} = \varepsilon_c$, which can be calculated from the derivative $\partial f_e^{\rm sm}(\varepsilon)/\partial\varepsilon = 0$, we obtain

$$\varepsilon_{\rm peak} = \varepsilon_{\rm min}\left(1 + \frac{1}{\delta}\right). \qquad (43)$$

For instance, for the example shown in Figure 8, the energy ratio is $\varepsilon_{\rm peak} = \varepsilon_{\rm min}(1 + 1/\delta) = 4/3 = 1.333$ for $\delta = 3$. For steeper slopes δ the ratio becomes smaller, such as $\varepsilon_{\rm peak} = \varepsilon_{\rm min}(1 + 1/\delta) = 9/8 = 1.125$ for $\delta = 8$.

We can now analytically calculate the functional form of the total number of electrons above a cutoff energy of ε_c:

$$F^{\rm sm}(\varepsilon \geqslant \varepsilon_{\rm min}) = \int_{\varepsilon_{\rm min}}^{\infty} f_e(\varepsilon)\left(1 - \frac{\varepsilon_c}{\varepsilon}\right)d\varepsilon = F(\varepsilon \geqslant \varepsilon_c)\left(\frac{1}{1+\gamma}\right) \quad (\text{electrons s}^{-1}), \qquad (44)$$

where the integration of $F(\varepsilon \geqslant \varepsilon_c)$ produces a simple multiplication factor $1/(1 + \gamma)$ that depends on the spectral slope γ of the photon spectrum only.

Similarly, we can analytically calculate the power $F^{\rm sm}(\varepsilon \geqslant \varepsilon_c)$ in nonthermal electrons above this cutoff energy:

$$P^{\rm sm}(\varepsilon \geqslant \varepsilon_{\rm min}) = \int_{\varepsilon_c}^{\infty} f_e(\varepsilon)\,\varepsilon\left(1 - \frac{\varepsilon_c}{\varepsilon}\right)d\varepsilon = P(\varepsilon \geqslant \varepsilon_c)\,\frac{1}{\gamma} \quad (\text{erg s}^{-1}), \qquad (45)$$

where the integration of $P(\varepsilon \geqslant \varepsilon_c)$ produces a similar multiplication factor $(1/\gamma)$ that depends on the spectral slope γ of the photon spectrum only. Since the correction of the sharply peaked electron injection function by a smoothed function depends on the power-law slope γ, we expect a change in the energy dependence of the distribution functions.

The smooth definition of the electron injection function affects also the value of the low-energy cutoff for the electron number model, since the total number of electrons N_e (Equation (6)) changes as

$$N_e = F(\varepsilon \geqslant \varepsilon_c)\left(\frac{1}{1+\gamma}\right)\tau_{\rm flare} \quad (\text{electrons}), \qquad (46)$$

and the resulting low-energy cutoff is modified by the factor $1/(1 + \gamma)$, compared with Equation (9), i.e.,

$$\varepsilon_{\rm en} = \epsilon_1\left[\frac{n_{e0}\,L_{10}^3\,q_{\rm geo}\,\epsilon_1}{0.72\,\gamma^2(\gamma^2 - 1)\,I_1\,\tau_{\rm flare}}\right]^{-1/\gamma} \quad (\text{keV}). \qquad (47)$$

Thus, the smooth electron injection function causes this modification in the calculation of the low-energy cutoff of the electron number model, but it does not affect the time-of-flight model (Equation (20)), the warm target model (Equation (28)), or the cross-over model (Equation (33)), since these other models do not directly depend on the chosen electron injection function. Future studies may fit the smoothed electron injection function (Equation (41)) in order to obtain a more accurate estimate of flare energies.

Appendix B
Parameter Dependence of the Low-energy Cutoff

B.1. The Electron Number Model

The input parameters of our low-energy cutoff models affect the final result of the low-energy cutoff value ε in a specific way for each parameter. In Table 1 (based on the parameter distributions shown in Figure 3) we list the mean and standard deviations $x_{\rm mean} \pm \sigma$ of each observed variable ($x = T_e$, γ, L, $\tau_{\rm flare}$, EM, I_1, n_e, n_{e0}), which can be characterized by the variance ratio $\sigma/x_{\rm mean}$, found to range from $\sigma_\gamma/\gamma = 1.20$ (for spectral slopes) up to a factor of $\sigma_{\rm EM}/{\rm EM} = 11.0$ (for emission measures) (Table 1).

We investigate now how these typical parameter variations affect the typical values of the resulting low-energy cutoffs ε. We start with the electron number model (Equation (9)):

$$\varepsilon_{\rm en} = \epsilon_1\left[\frac{n_{e0}\,L_{10}^3\,q_{\rm geo}\,\epsilon_1}{0.72\,\gamma^2(\gamma - 1)\,I_1\,\tau_{\rm flare}}\right]^{-1/\gamma} \quad (\text{keV}). \qquad (48)$$

Denoting the mean value of the preflare electron density with n_{e0} and the value of a standard deviation higher with $\tilde{n}_{e0}$ (with $[\tilde{n}_{e0}/n_{e0}] = 6.34$ according to Table 1), the corresponding low-energy cutoff value $\tilde{\varepsilon}_{en}$ is

$$\frac{\tilde{\varepsilon}_{en}}{\varepsilon_{en}} = \left[\frac{\tilde{n}_{e0}}{n_{e0}}\right]^{-1/\gamma} = [6.34]^{-1/7} = 0.77, \quad (49)$$

which means that the low-energy cutoff value $\tilde{\varepsilon}_{en}$ comes out to be 23% lower for a preflare electron density that is a standard deviation higher than the mean value. This value can be considered as an upper limit of the uncertainty of the low-energy cutoff value if all the variance in the electron density measurements is due to measurement errors in the electron density. Practically, since the obtained mean value is $\varepsilon_{en} = 10.8 \pm 7.5$ keV (Figure 4(a)), this uncertainty is 0.23×10.8 keV ≈ 2.5 keV.

Next we investigate the uncertainty caused by the non-thermal flux I_1. Denoting the mean value with I_1 and the value of a standard deviation higher with $\tilde{I}_1$ (with $[\tilde{I}_1/I_1] = 6.40$ according to Table 1), the corresponding low-energy cutoff value $\tilde{\varepsilon}_{en}$ is

$$\frac{\tilde{\varepsilon}_{en}}{\varepsilon_{en}} = \left[\frac{I_1}{\tilde{I}_1}\right]^{-1/\gamma} = [1./6.40]^{-1/7} = 1.30, \quad (50)$$

which means that the low-energy cutoff value $\tilde{\varepsilon}_{en}$ comes out to be 30% higher for a nonthermal flux that is a standard deviation higher than the mean value. This value indicates an uncertainty of 0.30×10.8 keV ≈ 3.2 keV, which is an upper limit of the uncertainty if all variance is due to measurement errors of the nonthermal flux.

Next we investigate the uncertainty due to the flare duration τ_{flare}. Denoting the mean value with τ_{flare} and the value of a standard deviation higher with $\tilde{\tau}_{flare}$ (with $[\tilde{\tau}_{flare}/\tau_{flare}] = 1.84$ according to Table 1), the corresponding low-energy cutoff value $\tilde{\varepsilon}_{en}$ is

$$\frac{\tilde{\varepsilon}_{en}}{\varepsilon_{en}} = \left[\frac{\tau_{flare}}{\tilde{\tau}_{flare}}\right]^{-1/\gamma} = \left[\frac{1}{1.84}\right]^{-1/7} = 1.15, \quad (51)$$

which means that the low-energy cutoff value $\tilde{\varepsilon}_{en}$ comes out to be 15% higher for a flare duration that is a standard deviation higher than the mean value. This value indicates an uncertainty of 0.15×10.8 keV ≈ 1.6 keV, which is an upper limit of the uncertainty if all variance is due to measurement errors of the flare duration.

Next we investigate the uncertainty due to the flare length scale L. Denoting the mean value with L and the value of a standard deviation higher with $\tilde{L}$ (with $[\tilde{L}/L] = 1.55$ according to Table 1), the corresponding low-energy cutoff value $\tilde{\varepsilon}_{en}$ is

$$\frac{\tilde{\varepsilon}_{en}}{\varepsilon_{en}} = \left[\frac{\tilde{L}^3}{L^3}\right]^{-1/\gamma} = [1.55^3]^{-1/7} = 0.83, \quad (52)$$

which means that the low-energy cutoff value $\tilde{\varepsilon}_{en}$ comes out to be 17% lower for a length scale that is a standard deviation larger than the mean value. This value indicates an uncertainty of 0.17×10.8 keV ≈ 1.8 keV, which is an upper limit of the uncertainty if all variance is due to measurement errors of the flare length scale.

Next we investigate the uncertainty due to the spectral slope γ. Denoting the mean value with γ and the value of a standard deviation higher with $\tilde{\gamma}$ (with $[\tilde{\gamma}/\gamma] = 1.20$ according to Table 1), the corresponding low-energy cutoff value $\tilde{\varepsilon}_{en}$ is

$$\frac{\tilde{\varepsilon}_{en}}{\varepsilon_{en}} = \left[\frac{\gamma^2(\gamma-1)}{\tilde{\gamma}^2(\tilde{\gamma}-1)}\right]^{-1/\gamma} = [1.63]^{-1/7} = 0.93, \quad (53)$$

which means that the low-energy cutoff value $\tilde{\varepsilon}_{en}$ comes out to be 7% lower for a spectral index scale that is a standard deviation larger than the mean value. This value indicates an uncertainty of 0.07×10.8 keV ≈ 0.8 keV, which is an upper limit of the uncertainty if all variance is due to measurement errors of the spectral slope.

Finally, we investigate also the uncertainty due to the geometric parameter $q_{geo} = 1/4$, which is assumed for the ratio of the flare arcade volume with respect to an encompassing cube. Denoting the mean value with q_{geo} and the value of a factor 2 higher with $\tilde{q}_{geo}$ (i.e., $[\tilde{\gamma}/\gamma] = 2$), the corresponding low-energy cutoff value $\tilde{\varepsilon}_{en}$ is

$$\frac{\tilde{\varepsilon}_{en}}{\varepsilon_{en}} = \left[\frac{\tilde{q}_{geo}}{q_{geo}}\right]^{-1/\gamma} = [2]^{-1/7} = 0.91, \quad (54)$$

which means that the low-energy cutoff value $\tilde{\varepsilon}_{en}$ comes out to be 9% lower for a geometry factor that is a factor 2 larger than the mean value. This value indicates an uncertainty of 0.09×10.8 keV ≈ 1.0 keV, which is an upper limit on the uncertainty of the geometry factor.

In summary, upper limits of the uncertainties σ_x of the low-energy cutoff ε_{en} in our electron number model are estimated (in decreasing order) from the following parameters: the nonthermal flux I_1 (i.e., $\sigma_{I1} < 30\%$ of the low-energy cutoff value), preflare electron density n_{e0} (<23%), flare length scale τ_{flare} (<17%), flare duration τ_{flare} (<15%), geometric model q_{geo} (<9%), and spectral index γ (<7%). In these estimates we make the assumption that the variance of the values is entirely caused by measurement errors, which constitute upper limits on the uncertainties of the low-energy cutoff values.

B.2. The Time-of-flight Model

We proceed now to our second model, the so-called time-of-flight model, which depends on two parameters only, the length scale L and the mean electron density n_e during flares (Equation (20)):

$$e_{tof} \approx 28\left(\frac{L}{10^{10}\text{ cm}}\right)^{1/2}\left(\frac{n_e}{10^{10}\text{ cm}^{-3}}\right)^{1/2} \quad \text{(keV)}. \quad (55)$$

Similarly to the previous method, we investigate the uncertainty due to the length scale L. Denoting the mean value with L and the value of a standard deviation higher with $\tilde{L}$ (with $[\tilde{L}/L] = 1.55$ according to Table 1), the corresponding low-energy cutoff value $\tilde{\varepsilon}_{en}$ is

$$\frac{\tilde{\varepsilon}_{en}}{\varepsilon_{en}} = \left[\frac{\tilde{L}}{L}\right]^{1/2} = [1.55]^{1/2} = 1.24, \quad (56)$$

which means that the low-energy cutoff value $\tilde{\varepsilon}_{\rm en}$ comes out to be 24% higher for a length scale that is a standard deviation larger than the mean value. Using the distribution shown in Figure 4(b), i.e., $\varepsilon_{\rm tof} = 9.8 \pm 9.5$ keV. This value indicates a mean uncertainty of $0.24 \times 9.8\,{\rm keV} \approx 2.4$ keV, which is an upper limit of the uncertainty when all variance is due to measurement errors of the length scale.

Denoting the mean value of the flare electron density with n_e and the value of a standard deviation higher with $\tilde{n}_e$ (with $[\tilde{n}_e/n_e] = 3.69$ according to Table 1), the corresponding low-energy cutoff value $\tilde{\varepsilon}_{\rm en}$ is

$$\frac{\tilde{\varepsilon}_{\rm en}}{\varepsilon_{\rm en}} = \left[\frac{\tilde{n}_e}{n_e}\right]^{1/2} = [3.69]^{1/2} = 1.92, \quad (57)$$

which means that the low-energy cutoff value $\tilde{\varepsilon}_{\rm en}$ comes out to be 92% higher for a flare electron density that is a standard deviation higher than the mean value. This value can be considered as an upper limit of the uncertainty of the low-energy cutoff value if all the variance in the electron density measurements is due to measurement errors in the electron density. Practically, since the obtained mean value is $\varepsilon_{\rm en} = 9.8 \pm 9.5$ keV (Figure 4(b)), this uncertainty is $0.92 \times 10.8\,{\rm keV} \approx 9.0$ keV. This large uncertainty implies a high sensitivity of the low-energy cutoff on the flare density, while it is substantially less sensitive to the flare length scale. It is therefore imperative to measure the flare density accurately, which requires detailed DEM analysis.

B.3. The Warm Target Model

Finally, we investigate the parameter dependence of the warm target model, which in its simplest form (Equation (28)) is

$$\varepsilon_{\rm wt} \approx (\xi + 2) k_{\rm B} T_e = \delta\, k_{\rm B} T_e \; = (\gamma + 1) k_{\rm B} T_e, \quad (58)$$

where $\xi = \gamma - 1$ is the power-law slope of the source-integrated mean electron flux spectrum (see Equations (8)–(10) in Kontar et al. 2015), and T_e is the temperature of the warm target plasma. Denoting the mean value of the spectral index with γ and the value of a standard deviation higher with $\tilde{\gamma}$ (with $[\tilde{\gamma}/\gamma] = 1.20$ according to Table 1), the corresponding low-energy cutoff value $\tilde{\varepsilon}_{\rm en}$ is

$$\frac{\tilde{\varepsilon}_{\rm en}}{\varepsilon_{\rm en}} = \left[\frac{\tilde{\gamma} + 1}{\gamma + 1}\right] = 1.18 \quad (59)$$

which means that the low-energy cutoff value $\tilde{\varepsilon}_{\rm en}$ comes out to be 18% higher for a spectral index that is a standard deviation higher than the mean value. This value can be considered as an upper limit of the uncertainty of the low-energy cutoff value if all the variance in the spectral index measurements is due to measurement errors in the electron density. Practically, since the obtained mean value is $\varepsilon_{\rm en} = 9.9 \pm 4.8$ keV (Figure 4(c)), this uncertainty is $0.18 \times 9.9\,{\rm keV} \approx 2.0$ keV.

The temperature dependence can be calculated by denoting the mean value of the spectral index with T_e and the value of a standard deviation higher with $\tilde{T}_e$ (with $[\tilde{T}_e/T_e] = 1.40$ according to Table 1); the corresponding low-energy cutoff value $\tilde{\varepsilon}_{\rm en}$ is

$$\frac{\tilde{\varepsilon}_{\rm en}}{\varepsilon_{\rm en}} = \left[\frac{\tilde{T}_e}{T_e}\right] = 1.40 \quad (60)$$

which means that the low-energy cutoff value $\tilde{\varepsilon}_{\rm en}$ comes out to be 40% higher for a spectral index that is a standard deviation higher than the mean value. This value can be considered as an upper limit of the uncertainty of the low-energy cutoff value if all the variance in the spectral index measurements is due to measurement errors in the electron density. Practically, since the obtained mean value is $\varepsilon_{\rm en} = 9.9 \pm 4.8$ keV (Figure 4(c)), this uncertainty is $0.40 \times 9.9\,{\rm keV} \approx 4.0$ keV.

Thus, for the warm target model, uncertainties up to 18% of the low-energy cutoff could arise due to uncertainties in the spectral index, and uncertainties up to 40% of the low-energy cutoff could be caused by uncertainties in the temperature measurement.

ORCID iDs

Markus J. Aschwanden https://orcid.org/0000-0003-0260-2673
Natasha L. S. Jeffrey https://orcid.org/0000-0001-6583-1989

References

Aschwanden, M. J. 2004, Physics of the Solar Corona. An Introduction (Berlin: Springer and Praxis), 216
Aschwanden, M. J. 2007, ApJ, 661, 1242
Aschwanden, M. J. 2015, ApJ, 814, 19
Aschwanden, M. J. 2016, ApJ, 831, 105
Aschwanden, M. J. 2017, ApJ, 847, 27
Aschwanden, M. J. 2019, New Millennium Solar Physics, Vol. 458 (Berlin: Springer)
Aschwanden, M. J., Boerner, P., Ryan, D., et al. 2015, ApJ, 802, 53
Aschwanden, M. J., Caspi, A., Cohen, C. M. S., et al. 2017, ApJ, 836, 17
Aschwanden, M. J., & Gopalswamy, N. 2019, ApJ, 877, 149
Aschwanden, M. J., O'Flannagain, A., Caspi, A., et al. 2016, ApJ, 832, 27
Aschwanden, M. J., Xu, Y., & Jing, J. 2014, ApJ, 797, 50
Benz, A. O. 1993, Plasma Astrophysics. Kinetic Processes in Solar and Stellar Coronae (Dordrecht: Kluwer Academic), 45
Bian, N. H., Emslie, A. G., Stackhouse, D. J., & Kontar, E. P. 2014, ApJ, 796, 142
Brown, J. C. 1971, SoPh, 18, 489
Brown, J. C. 1974a, in IAU Symp. 57, Coronal Disturbances, ed. G. A. Newkirk Jr. (Dordrecht: Reidel), 395
Brown, J. C. 1974b, in IAU Symp. 57, Coronal Disturbances, ed. G. A. Newkirk Jr. (Dordrecht: Reidel), 523
Carmichael, H. 1964, in Proc. AAS-NASA Symp. NASA-SP 50, The Physics of Solar Flares, ed. W. N. Hess (Washington, DC: NASA Science and Technical Information Division), 451
Crosby, N. B., Aschwanden, M. J., & Dennis, B. 1993, SoPh, 143, 275
Culhane, J. L. 1969, MNRAS, 144, 375
Culhane, J. L., & Acton, L. 1970, MNRAS, 151, 141
Dennis, B. R. 1985, SoPh, 100, 465
Dulk, G. A., & Dennis, B. R. 1982, ApJ, 260, 875
Emslie, A. G., Dennis, B. R., & Shih, A. Y. 2012, ApJ, 759, 71
Galloway, R. K., MacKinnon, A. L., Kontar, E. P., & Helander, P. 2005, A&A, 438, 1107
Goncharov, P. R., KJuteev, B. V., Ozaki, T., & Sudo, S. 2010, PhPl, 17, 112313
Guo, J., Emslie, A. G., Kontar, E. P., et al. 2012a, A&A, 543, A53
Guo, J., Emslie, A. G., Massone, A. M., Piana, M., & PIana, M. 2012b, ApJ, 755, 32
Guo, J., Emslie, A. G., & Piana, M. 2013, ApJ, 766, 28
Hirayama, T. 1974, SoPh, 34, 323
Holman, G. D. 2003, ApJ, 586, 606
Holman, G. D., Aschwanden, M. J., Aurass, M. J., et al. 2011, SSRv, 159, 107
Hudson, H. S., Canfield, R. C., & Kane, S. R. 1978, SoPh, 60, 137

Ireland, J., Tolbert, A. K., Schwartz, R. A., Holman, G. D., & Dennis, B. R. 2013, ApJ, 769, 89
Jeffrey, N. L. S., Kontar, E. P., Bian, N. H., & Emslie, A. G. 2014, ApJ, 787, 86
Jeffrey, N. L. S., Kontar, E. P., & Emslie, A. G. 2015, A&A, 584, 89
Kontar, E. P., Jeffrey, N. L. S., & Emslie, A. G. 2019, ApJ, 871, 225
Kontar, E. P., Jeffrey, N. L. S., Emslie, A. G., & Bian, N. H. 2015, ApJ, 809, 35
Kopp, G., & Pneuman, G. W. 1976, SoPh, 50, 85
Lemen, J. R., Title, A. M., Akin, D. J., et al. 2012, SoPh, 275, 17
Lin, R. P., Dennis, B. R., Hurford, G. J., et al. 2002, SoPh, 210, 3
Pesnell, W. D., Thompson, B. J., & Chamberlin, P. C. 2011, SoPh, 275, 3
Scherrer, P. H., Schou, J., Bush, R. I., et al. 2012, SoPh, 275, 207
Somov, B. V. 2000, Cosmic Plasma Physics (Dordrecht: Kluwer)
Sturrock, P. A. 1966, Natur, 5050, 695
Xu, Y., Emslie, A. G., & Hurford, G. J. 2008, ApJ, 673, 576